

Angular Graph Fractional Fourier Transform: Theory and Application

Feiyue Zhao, Yangfan He, and Zhichao Zhang, *Member, IEEE*

Abstract—Graph spectral representations are fundamental in graph signal processing, offering a rigorous framework for analyzing and processing graph-structured data. The graph fractional Fourier transform (GFRFT) extends the classical graph Fourier transform (GFT) with a fractional-order parameter, enabling a flexible spectral analysis while preserving mathematical consistency. The angular graph Fourier transform (AGFT) introduces angular control via GFT eigenvector rotation; however, existing constructions fail to degenerate to the GFT at zero angle, which is a critical flaw that undermines theoretical consistency and interpretability. To resolve these complementary limitations—GFRFT’s lack of angular regulation and AGFT’s defective degeneracy—this study proposes an angular GFRFT (AGFRFT), a unified framework that integrates fractional order and angular spectral analyses with theoretical rigor. A degeneracy-friendly rotation matrix family ensures exact GFT degeneration at a zero angle, with two AGFRFT variants (I-AGFRFT and II-AGFRFT) defined as follows: rigorous theoretical analyses confirm their unitarity, invertibility, and smooth parameter dependence. Both support learnable joint parameterization of the angle and fractional order, enabling adaptive spectral processing for diverse graph signals. Extensive experiments on real-world data denoising, image denoising, and point cloud denoising demonstrate that AGFRFT outperforms GFRFT and AGFT in terms of spectral concentration, reconstruction quality, and controllable spectral manipulation, establishing a robust and flexible tool for integrated angular-fractional spectral analysis in graph signal processing.

Index Terms—Angular spectral analysis, degeneracy friendly rotation, denoising, graph fractional Fourier transform, learnable parameterization.

I. INTRODUCTION

This work was supported in part by the Open Foundation of Hubei Key Laboratory of Applied Mathematics (Hubei University) under Grant HBAM202404; in part by the Foundation of Key Laboratory of System Control and Information Processing, Ministry of Education under Grant Scip20240121; in part by the Foundation of Key Laboratory of Computational Science and Application of Hainan Province under Grant JSKX202401; in part by the Foundation of Key Laboratory of Numerical Simulation of Sichuan Provincial Universities under Grant KLNS–2024SZFZ005; and in part by the Startup Foundation for Introducing Talent of Nanjing Institute of Technology under Grant YKJ202214. (*Corresponding author: Zhichao Zhang.*)

Feiyue Zhao is with the School of Mathematics and Statistics, the Center for Applied Mathematics of Jiangsu Province, and the Jiangsu International Joint Laboratory on System Modeling and Data Analysis, Nanjing University of Information Science and Technology, Nanjing 210044, China (e-mail: 202511150010@nuist.edu.cn).

Yangfan He is with the School of Communication and Artificial Intelligence, School of Integrated Circuits, Nanjing Institute of Technology, Nanjing 211167, China (e-mail: Yangfan.He@njit.edu.cn).

Zhichao Zhang is with the School of Mathematics and Statistics, Nanjing University of Information Science and Technology, Nanjing 210044, China, with the Hubei Key Laboratory of Applied Mathematics, Hubei University, Wuhan 430062, China, with the Key Laboratory of System Control and Information Processing, Ministry of Education, Shanghai Jiao Tong University, Shanghai 200240, China, with the Key Laboratory of Computational Science and Application of Hainan Province, Hainan Normal University, Haikou 571158, China, and also with the Key Laboratory of Numerical Simulation of Sichuan Provincial Universities, School of Mathematics and Information Sciences, Neijiang Normal University, Neijiang 641000, China (e-mail: zzc910731@163.com).

GRAPH signal processing (GSP) has emerged as a foundational framework for analyzing non-Euclidean structured data [1]–[10], addressing the inherent limitations of traditional signal processing techniques that are tailored exclusively to regular grid signals (e.g., time series, images). Unlike classical methods, which rely on shift-invariance and uniform topology to enable rigorous spectral analysis, conventional signal processing tools cannot be directly extended to graph-structured data where signals are defined on irregular vertex sets with complex relational dependencies [11]–[13]. This critical gap has driven the rapid advancement of GSP, which generalizes core concepts of classical signal processing (e.g., Fourier transform, filtering, spectral decomposition) to the graph domain, thereby providing principled and interpretable tools for transforming, analyzing, and enhancing signals supported on graphs. As GSP gains growing utility in high-impact applications [14]–[19], including image processing, spatiotemporal sensor data analysis, and 3D point cloud denoising, the demand for more flexible and theoretically consistent spectral transformation methods has become increasingly pressing.

At the core of GSP lies the graph spectral representation, where graph signals are projected onto the eigenspace of a graph shift operator (e.g., an adjacency matrix) [20]–[25]. The resulting graph Fourier transform (GFT) reveals the intrinsic frequency components of the signals, thereby enabling efficient filtering, denoising, compression, and spectral analysis of graph-structured data [26]–[33]. The proven effectiveness of GFT across diverse graph signal processing tasks underscores the pivotal role of spectral representations in rigorous graph-based signal analysis. However, as the scale and complexity of graph-structured data increase, the limitations of conventional GFT become increasingly prominent, driving the need for spectral transforms with enhanced flexibility, adaptability, and interpretability that align with the demands of complex graph signal processing scenarios.

To address this demand, fractional spectral methods have been explored, with the graph fractional Fourier transform (GFRFT) extending the classical GFT by introducing a fractional-order parameter [34]–[42]. This parameter generates intermediate spectral domains that smoothly interpolate between the vertex and graph-frequency domains, providing an additional degree of freedom to enable finer spectral resolution and adaptive filtering. These capabilities surpass the analytical limits of conventional GFT while preserving mathematical rigor. However, GFRFT lacks mechanisms for angular manipulation of the spectral basis, which is a critical limitation in applications requiring continuous control over the spectral orientation. To mitigate this limitation, the angular graph Fourier transform (AGFT) was proposed to incorporate

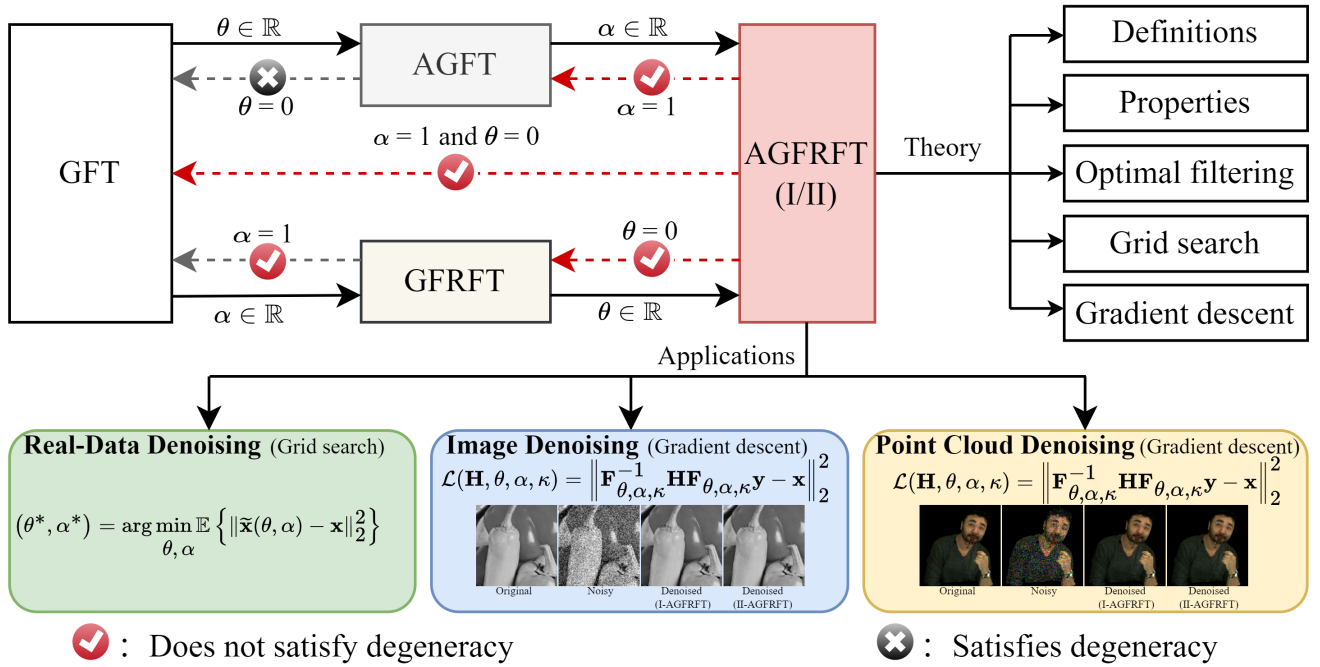


Fig. 1: Overview of the proposed AGFRFT framework and its applications.

angular control via the rotation of GFT eigenvectors based on prescribed angular parameters, adding another dimension of flexibility for spectral representation and controllable transformation domains [43]. Nevertheless, existing AGFT constructions typically fail to degenerate to the original GFT at zero angle, undermining both theoretical consistency and interpretability, and are not inherently integrated with fractional-order analysis, limiting adaptability in scenarios where both angular and fractional flexibility are essential.

To overcome these complementary limitations of GFRFT and AGFT, this paper introduces the angular GFRFT (AGFRFT), a unified framework that integrates fractional-order and angular spectral analysis while maintaining theoretical consistency and practical implementability. The overall architecture of the proposed AGFRFT framework is illustrated in Fig. 1, with its key contributions summarized as follows:

- We design a degeneracy-friendly rotation matrix family ensuring exact GFT reduction at zero angle, resolving conventional AGFT's consistency and interpretability flaws.
- We introduce two AGFRFT formulations (I-AGFRFT/II-AGFRFT) and rigorously analyze their core properties and smooth variation with both angular and fractional-order parameters.
- We provide a learnable angle-fractional order joint parametrization, enabling optimized spectral processing via standard gradient-based methods.
- We validate the framework via extensive experiments, demonstrating superiority over GFRFT and AGFT in spectral concentration, reconstruction quality, and controllable manipulation.

The remainder of this paper is organized as follows: Section II reviews preliminaries. Section III details the proposed AGFRFT framework. Section IV presents the experimental results and analysis. Finally, Section V concludes the paper and outlines future research directions. All the technical proofs of our theoretical results are relegated to the Appendix parts.

II. PRELIMINARIES

This section introduces the core GSP concepts that form the foundation of the proposed AGFRFT. We first review graph signals and shift operators, then cover GFT and GFRFT, and conclude with angular rotations in the graph spectral space and AGFT.

A. Graph Signals and Graph Shift Operators

Let $\mathcal{G} = (\mathcal{V}, \mathcal{E}, \mathbf{W})$ denote an undirected weighted graph, where \mathcal{V} is the set of N nodes, \mathcal{E} is the edge set, and $\mathbf{W} \in \mathbb{R}^{N \times N}$ is the weighted adjacency matrix. A graph signal $\mathbf{x} \in \mathbb{R}^N$ assigns a scalar value to each node of the graph [3], [15].

Graph shift operators (GSOs), such as the adjacency matrix \mathbf{A} , weighted adjacency \mathbf{W} , or graph Laplacian \mathbf{L} , encode the underlying graph structure and provide the foundation for spectral analysis [44].

B. Graph Fourier Transform (GFT)

Consider the eigendecomposition of a general GSO \mathbf{Z} :

$$\mathbf{Z} = \mathbf{U} \mathbf{\Lambda} \mathbf{U}^{-1} = \mathbf{U} \mathbf{\Lambda} \mathbf{U}^H, \quad (1)$$

where $\mathbf{\Lambda} = \text{diag}(\lambda_1, \dots, \lambda_N)$ contains the eigenvalues and $\mathbf{U} = [\mathbf{u}_1, \dots, \mathbf{u}_N]$ contains the corresponding eigenvectors. The graph Fourier transform of a signal \mathbf{x} is defined as

$$\hat{\mathbf{x}} = \mathbf{F} \mathbf{x}, \quad \mathbf{F} = \mathbf{U}^{-1} = \mathbf{U}^H. \quad (2)$$

The eigenvectors \mathbf{u}_k form an orthonormal basis spanning the graph spectral domain, enabling filtering, analysis, and representation of graph signals [26], [29].

C. Graph Fractional Fourier Transform (GFRFT)

The GFRFT introduces a fractional-order parameter $\alpha \in \mathbb{R}$, which interpolates between the vertex and graph-frequency domains:

$$\widehat{\mathbf{x}}^\alpha = \mathbf{F}^\alpha \mathbf{x}. \quad (3)$$

By varying α , one can flexibly control the spectral representation while remaining mathematically consistent with the GFT [34], [37].

D. Roll, Pitch, and Yaw Rotation Matrices

Assume that $\mathbf{R}_{M \times M}$ is an $M \times M$ orthogonal matrix, then the matrices

$$\mathbf{R}_{2M \times 2M} = \frac{1}{\sqrt{2}} \begin{pmatrix} \mathbf{R}_{M \times M} & \mathbf{R}_{M \times M} \\ -\mathbf{R}_{M \times M}^\top & \mathbf{R}_{M \times M}^\top \end{pmatrix}, \quad (4)$$

$$\mathbf{R}_{(2M+1) \times (2M+1)}^{\text{roll}} = \frac{1}{\sqrt{2}} \begin{pmatrix} \sqrt{2} & \mathbf{0}_{1 \times M} & \mathbf{0}_{1 \times M} \\ \mathbf{0}_{M \times 1} & \mathbf{R}_{M \times M} & \mathbf{R}_{M \times M} \\ \mathbf{0}_{M \times 1} & -\mathbf{R}_{M \times M}^\top & \mathbf{R}_{M \times M}^\top \end{pmatrix}, \quad (5)$$

$$\mathbf{R}_{(2M+1) \times (2M+1)}^{\text{pitch}} = \frac{1}{\sqrt{2}} \begin{pmatrix} \mathbf{R}_{M \times M} & \mathbf{0}_{M \times 1} & -\mathbf{R}_{M \times M}^\top \\ \mathbf{0}_{1 \times M} & \sqrt{2} & \mathbf{0}_{1 \times M} \\ \mathbf{R}_{M \times M} & \mathbf{0}_{M \times 1} & \mathbf{R}_{M \times M}^\top \end{pmatrix}, \quad (6)$$

$$\mathbf{R}_{(2M+1) \times (2M+1)}^{\text{yaw}} = \frac{1}{\sqrt{2}} \begin{pmatrix} \mathbf{R}_{M \times M} & \mathbf{R}_{M \times M} & \mathbf{0}_{M \times 1} \\ -\mathbf{R}_{M \times M}^\top & \mathbf{R}_{M \times M}^\top & \mathbf{0}_{M \times 1} \\ \mathbf{0}_{1 \times M} & \mathbf{0}_{1 \times M} & \sqrt{2} \end{pmatrix}. \quad (7)$$

are both orthogonal matrices, where $\mathbf{0}_{M \times 1}$ and $\mathbf{0}_{1 \times M}$ are $M \times 1$ and $1 \times M$ zero vectors, respectively, and $\mathbf{R}_{M \times M}^\top := [r_{M+1-i, j}]_{i, j=1, 2, \dots, M}$ is defined by upside down the matrix $\mathbf{R}_{M \times M} = [r_{i, j}]_{i, j=1, 2, \dots, M}$.

The 2×2 rotation matrix reads

$$\mathbf{R}_{2 \times 2}^\theta = \begin{pmatrix} \cos \theta & \sin \theta \\ -\sin \theta & \cos \theta \end{pmatrix}, \quad (8)$$

where $\theta \in [0, 2\pi]$. The following three basic rotation matrices that rotate vectors by a roll, pitch, or yaw angle θ about the x -, y -, or z -axis, in three dimensions:

$$\mathbf{R}_{3 \times 3}^{\text{roll}, \theta} = \begin{pmatrix} 1 & 0 & 0 \\ 0 & \cos \theta & \sin \theta \\ 0 & -\sin \theta & \cos \theta \end{pmatrix}, \quad (9)$$

$$\mathbf{R}_{3 \times 3}^{\text{pitch}, \theta} = \begin{pmatrix} \cos \theta & 0 & -\sin \theta \\ 0 & 1 & 0 \\ \sin \theta & 0 & \cos \theta \end{pmatrix}, \quad (10)$$

$$\mathbf{R}_{3 \times 3}^{\text{yaw}, \theta} = \begin{pmatrix} \cos \theta & \sin \theta & 0 \\ -\sin \theta & \cos \theta & 0 \\ 0 & 0 & 1 \end{pmatrix}, \quad (11)$$

where $\theta \in [0, 2\pi]$ [45]–[48].

Due to Eqs. (4), (5), (8) and (9), the $N \times N$ rotation matrix $\mathbf{R}_{N \times N}^{\text{roll}, \theta}$ that rotates vectors by a roll angle θ about the x -axis,

abbreviated as the $N \times N$ roll rotation matrix, can be computed iteratively as

$$\mathbf{R}_{2M \times 2M}^{\text{roll}, \theta} = \frac{1}{\sqrt{2}} \begin{pmatrix} \mathbf{R}_{M \times M}^{\text{roll}, \theta} & \mathbf{R}_{M \times M}^{\text{roll}, \theta} \\ -(\mathbf{R}_{M \times M}^{\text{roll}, \theta})^\top & (\mathbf{R}_{M \times M}^{\text{roll}, \theta})^\top \end{pmatrix} \quad (12)$$

and

$$\begin{aligned} \mathbf{R}_{(2M+1) \times (2M+1)}^{\text{roll}, \theta} \\ = \frac{1}{\sqrt{2}} \begin{pmatrix} \sqrt{2} & \mathbf{0}_{1 \times M} & \mathbf{0}_{1 \times M} \\ \mathbf{0}_{M \times 1} & \mathbf{R}_{M \times M}^{\text{roll}, \theta} & \mathbf{R}_{M \times M}^{\text{roll}, \theta} \\ \mathbf{0}_{M \times 1} & -(\mathbf{R}_{M \times M}^{\text{roll}, \theta})^\top & (\mathbf{R}_{M \times M}^{\text{roll}, \theta})^\top \end{pmatrix} \end{aligned} \quad (13)$$

for even $N = 2M$ and odd $N = 2M + 1$, respectively. Similarly, the $N \times N$ pitch and yaw rotation matrices $\mathbf{R}_{N \times N}^{\text{pitch}, \theta}$ and $\mathbf{R}_{N \times N}^{\text{yaw}, \theta}$ can be computed iteratively as

$$\mathbf{R}_{2M \times 2M}^{\text{pitch}, \theta} = \frac{1}{\sqrt{2}} \begin{pmatrix} \mathbf{R}_{M \times M}^{\text{pitch}, \theta} & \mathbf{R}_{M \times M}^{\text{pitch}, \theta} \\ -(\mathbf{R}_{M \times M}^{\text{pitch}, \theta})^\top & (\mathbf{R}_{M \times M}^{\text{pitch}, \theta})^\top \end{pmatrix}, \quad (14)$$

$$\begin{aligned} \mathbf{R}_{(2M+1) \times (2M+1)}^{\text{pitch}, \theta} \\ = \frac{1}{\sqrt{2}} \begin{pmatrix} \mathbf{R}_{M \times M}^{\text{pitch}, \theta} & \mathbf{0}_{M \times 1} & -(\mathbf{R}_{M \times M}^{\text{pitch}, \theta})^\top \\ \mathbf{0}_{1 \times M} & \sqrt{2} & \mathbf{0}_{1 \times M} \\ \mathbf{R}_{M \times M}^{\text{pitch}, \theta} & \mathbf{0}_{M \times 1} & (\mathbf{R}_{M \times M}^{\text{pitch}, \theta})^\top \end{pmatrix} \end{aligned} \quad (15)$$

and

$$\mathbf{R}_{2M \times 2M}^{\text{yaw}, \theta} = \frac{1}{\sqrt{2}} \begin{pmatrix} \mathbf{R}_{M \times M}^{\text{yaw}, \theta} & \mathbf{R}_{M \times M}^{\text{yaw}, \theta} \\ -(\mathbf{R}_{M \times M}^{\text{yaw}, \theta})^\top & (\mathbf{R}_{M \times M}^{\text{yaw}, \theta})^\top \end{pmatrix}, \quad (16)$$

$$\begin{aligned} \mathbf{R}_{(2M+1) \times (2M+1)}^{\text{yaw}, \theta} \\ = \frac{1}{\sqrt{2}} \begin{pmatrix} \mathbf{R}_{M \times M}^{\text{yaw}, \theta} & \mathbf{R}_{M \times M}^{\text{yaw}, \theta} & \mathbf{0}_{M \times 1} \\ -(\mathbf{R}_{M \times M}^{\text{yaw}, \theta})^\top & (\mathbf{R}_{M \times M}^{\text{yaw}, \theta})^\top & \mathbf{0}_{M \times 1} \\ \mathbf{0}_{1 \times M} & \mathbf{0}_{1 \times M} & \sqrt{2} \end{pmatrix}, \end{aligned} \quad (17)$$

respectively. Here, $\mathbf{R}_{2M \times 2M}^{\text{roll}, \theta} = \mathbf{R}_{2M \times 2M}^{\text{pitch}, \theta} = \mathbf{R}_{2M \times 2M}^{\text{yaw}, \theta} = \mathbf{R}_{2M \times 2M}^\theta$.

Notably, the prototype matrices (Eqs. (8)–(11)), specifically designed for $N = 3$, naturally degenerate to the identity matrix \mathbf{I}_3 at $\theta = 0$ (direct substitution of $\cos 0 = 1$ and $\sin 0 = 0$ yields \mathbf{I}_3). However, this critical degeneracy property is not preserved by the recursive high-dimensional rotation matrices (Eqs. (12)–(17)) when $N \geq 4$.

E. Angular Graph Fourier Transform (AGFT)

Let $\mathbf{R}_N^{\text{axis}}(\theta)$ be any orthogonal rotation matrix generated by one of the families above. Define the rotated eigenbasis

$$\mathbf{U}_\theta = \mathbf{R}_N^{\text{axis}}(\theta) \mathbf{U}, \quad \mathbf{U}_\theta^H \mathbf{U}_\theta = \mathbf{I}. \quad (18)$$

The angular graph Fourier transform (AGFT) of a graph signal \mathbf{x} associated with angle $\theta \in [0, 2\pi]$ is

$$\widehat{\mathbf{x}}_\theta = \mathbf{F}_\theta \mathbf{x}, \quad \mathbf{F}_\theta = \mathbf{U}_\theta^H. \quad (19)$$

AGFT retains unitarity for any fixed θ [43]. However, when high-dimensional rotation matrices $\mathbf{R}_N^{\text{axis}}(\theta)$ is taken from the recursive families above, one generally has $\mathbf{F}_{\theta=0} \neq \mathbf{U}^H$, i.e., AGFT does not revert to the original GFT at zero angle. This lack of degeneracy undermines interpretability and motivates the degeneracy-friendly construction developed in the next section.

TABLE I: Comparison of different graph spectral transforms.

Method	Fractional order	Angular control	Degeneracy to GFT	Periodicity	Invertibility	Remarks
GFRFT [34]	Yes	No	Yes	No	Yes	Spectral function extension of GFT
AGFT [43] (existing)	No	Yes	No	No	Yes	Rotation-based, inconsistent at zero angle
Corrected AGFT (proposed)	No	Yes	Yes	Yes	Yes	Degeneracy-friendly rotation matrices
AGFRFT (proposed)	Yes	Yes	Yes	Unknown	Yes	Unified framework (Type I/II)

III. ANGULAR GRAPH FRACTIONAL FOURIER TRANSFORM (AGFRFT)

This section elaborates on the proposed AGFRFT. We first motivate integrating angular and fractional degrees of freedom to address limitations of existing graph spectral transforms, then introduce a degeneracy-friendly rotation matrix family ensuring exact GFT degeneration, formulate two concrete AGFRFT variants (Type I and Type II), establish their fundamental theoretical properties, and finally derive explicit, computationally tractable expressions for the derivatives required to learn the angular and fractional parameters.

A. Motivation and Concept

The GFT provides a fixed orthonormal spectral basis determined by a graph shift operator (GSO). The GFRFT extends GFT by a fractional-order parameter α , enabling intermediate spectral domains and more flexible spectral analysis. Independently, AGFT rotate the GFT eigenbasis by an angular parameter θ to provide additional spectral degrees of freedom. However, many commonly used AGFT rotation constructions employ angle-independent equal-weight block combinations (e.g. $\frac{1}{\sqrt{2}} \begin{pmatrix} \mathbf{I} & \mathbf{I} \\ -\mathbf{I} & \mathbf{I} \end{pmatrix}$) in their recursion; as a result they fail to degenerate to the original GFT at $\theta = 0$ (a structural “no-go”). This undermines interpretability and consistency: a transform that purports to be an angular generalization should recover GFT when the angle vanishes.

Beyond overcoming the limitations of conventional angular graph transforms in distinguishing high-dimensional rotations, a principal design objective of the AGFRFT is to incorporate adaptive parameter tuning for practical applications. Unlike fixed-transform methods, the parameters θ and α are conceived as inherently tunable. This design enables the AGFRFT to function as a generalized, parameterized framework, where these parameters can be adjusted to optimize performance for specific signals or tasks, thereby facilitating highly tailored spectral processing.

Our objective is to unify fractional and angular control while preserving the following desiderata:

- **Degeneration:** at $\theta = 0$ the angular mechanism must reduce to the identity so that $\text{AGFRFT}|_{\theta=0} = \text{GFRFT}$.
- **Group structure:** each rotation $\mathbf{R}_N^{\text{axis}}(\theta)$ should lie in $SO(N)$ (orthogonal with determinant +1) for every θ .
- **Differentiability:** $\theta \mapsto \mathbf{R}_N^{\text{axis}}(\theta)$ and the resulting AGFRFT operators should be sufficiently smooth to admit gradient-based optimization of θ and α .

TABLE I concisely summarizes the key attributes of representative graph spectral transforms, clearly illustrating how the proposed AGFRFT unifies fractional-order flexibility and angular control while resolving the degeneracy

inconsistency of conventional AGFT and the lack of angular manipulation in GFRFT.

B. Degeneracy-Friendly Rotation Matrix Family

We introduce a recursively constructed family of rotation matrices that is *degeneracy-friendly* (reduces to identity at zero rotation) and distinguishes three axes (yaw, pitch, roll) for $N = 2^k$ dimensions.

Notation: Let $\mathbf{P}_M \in \mathbb{R}^{M \times M}$ denote the anti-diagonal permutation matrix (ones on the anti-diagonal). For any $\mathbf{X} \in \mathbb{R}^{M \times M}$, define its *diamond* (double-flip) by

$$\mathbf{X}^\diamond := \mathbf{P}_M \mathbf{X} \mathbf{P}_M.$$

Note that $\mathbf{P}_M^\top = \mathbf{P}_M = \mathbf{P}_M^{-1}$ and if $\mathbf{X} \in O(M)$ then $\mathbf{X}^\diamond \in O(M)$ with $\det(\mathbf{X}^\diamond) = \det(\mathbf{X})$.

Block rotation primitives: For integer $M \geq 1$ and angle $\phi \in \mathbb{R}$ define the even-dimensional block rotation (a direct sum of two-dimensional Givens blocks)

$$\mathbf{S}_M(\phi) := \begin{pmatrix} \cos \phi \mathbf{I}_M & \sin \phi \mathbf{I}_M \\ -\sin \phi \mathbf{I}_M & \cos \phi \mathbf{I}_M \end{pmatrix} \in SO(2M),$$

and for the odd-dimensional case define three block rotations acting on the block layout $(M, 1, M)$:

$$\mathbf{T}_M^{(1,2)}(\phi) := \begin{pmatrix} \cos \phi \mathbf{I}_M & \sin \phi \mathbf{I}_M & \mathbf{0} \\ -\sin \phi \mathbf{I}_M & \cos \phi \mathbf{I}_M & \mathbf{0} \\ \mathbf{0} & \mathbf{0} & 1 \end{pmatrix} \in SO(2M+1),$$

and similarly $\mathbf{T}_M^{(1,3)}(\phi)$, $\mathbf{T}_M^{(2,3)}(\phi)$ for the other two block-pair rotations. Each of these satisfies $\mathbf{S}_M(0) = \mathbf{I}_{2M}$ and $\mathbf{T}_M^{(\cdot)}(0) = \mathbf{I}_{2M+1}$.

Axis-dependent exponential map for high-dimensional distinction: To ensure that the yaw, pitch, and roll rotation families remain distinct in $N = 2^k$ dimensions, we introduce axis-dependent skew-symmetric matrices $\mathbf{J}_{\text{roll}}, \mathbf{J}_{\text{yaw}}, \mathbf{J}_{\text{pitch}} \in \mathbb{R}^{N \times N}$ (which satisfies $\mathbf{J}^\top = -\mathbf{J}$) with different sparsity patterns. These matrices are defined as

$$(\mathbf{J}_{\text{roll}})_{i,j} = \begin{cases} -1, & j = i + 1 \\ 1, & i = j + 1, \quad i, j = 1, \dots, N - 1, \\ 0, & \text{otherwise} \end{cases}$$

$$(\mathbf{J}_{\text{yaw}})_{i,j} = \begin{cases} -1, & j = i + 1, \quad i \text{ odd} \\ 1, & i = j + 1, \quad i \text{ odd}, \\ 0, & \text{otherwise} \end{cases}$$

$$(\mathbf{J}_{\text{pitch}})_{i,j} = \begin{cases} -1, & j = i + 1, \quad i \text{ even} \\ 1, & i = j + 1, \quad i \text{ even}. \\ 0, & \text{otherwise} \end{cases}$$

The corresponding rotation in high dimensions is obtained by applying the matrix exponential as a small perturbation after the block-diagonal rotations:

$$\mathbf{R} = \mathbf{R}_{\text{block}} \exp(\phi \mathbf{J}), \quad (20)$$

where angle $\phi \in \mathbb{R}$ controls the magnitude of the perturbation. This design ensures three properties:

- **Axis separation:** Different sparsity patterns prevent yaw, pitch, and roll families from collapsing onto each other in higher dimensions.
- **Orthogonality preservation:** As \mathbf{J} is skew-symmetric, $\exp(\phi \mathbf{J})$ is guaranteed to be orthogonal (Proof see Appendix A).
- **Physical Interpretability:** The sparsity patterns of the skew-symmetric matrices \mathbf{J}_{roll} , $\mathbf{J}_{\text{pitch}}$, and \mathbf{J}_{yaw} directly reflect the adjacent coupling inherent in physical rotations. In 3D, each elemental rotation (roll, pitch, yaw) acts only on two adjacent axes. This adjacency principle is preserved in our construction: each \mathbf{J} -matrix couples only specific pairs of adjacent dimensions (e.g., odd or even indices), maintaining a clear distinction between rotation types. The pattern naturally extends to higher dimensions ($N = 2^k$), ensuring that high-dimensional rotations remain physically interpretable as compositions of intuitive, low-dimensional transformations.

In this way, the exponential map serves as a controlled perturbation that maintains the geometric and physical meaning of the rotations while distinguishing axes in high-dimensional spaces.

Recursive construction: Let $\phi : \mathbb{R} \rightarrow \mathbb{R}$ be C^1 with $\phi(0) = 0$, e.g., $\phi(\theta) = \kappa\theta$.

- Base cases:

$$\begin{aligned} \mathbf{R}_1(\theta) &= 1, \\ \mathbf{R}_2(\theta) &= \begin{pmatrix} \cos \theta & \sin \theta \\ -\sin \theta & \cos \theta \end{pmatrix}, \\ \mathbf{R}_3^{\text{yaw}}(\theta) &= \begin{pmatrix} \cos \theta & \sin \theta & 0 \\ -\sin \theta & \cos \theta & 0 \\ 0 & 0 & 1 \end{pmatrix}. \end{aligned}$$

Similarly define base 3D blocks for pitch and roll.

- If $N = 2M$ is even:

$$\begin{aligned} \mathbf{R}_{2M}^{\text{axis}}(\theta) &= \text{blkdiag}(\mathbf{R}_M(\theta), \mathbf{R}_M^\circ(\theta)) \\ &\quad \times \mathbf{S}_M(\phi(\theta)) \times \exp(\phi(\theta) \mathbf{J}_{\text{axis}}(2M)), \end{aligned}$$

where $\text{axis} \in \{\text{yaw}, \text{pitch}, \text{roll}\}$ and \mathbf{J}_{axis} ensures axis distinction.

- If $N = 2M + 1$ is odd, define axis-dependent variants:

$$\begin{aligned} \mathbf{R}_{2M+1}^{\text{yaw}}(\theta) &= \text{blkdiag}(\mathbf{R}_M, \mathbf{R}_M^\circ, 1) \mathbf{T}_M^{(1,2)}(\phi), \\ \mathbf{R}_{2M+1}^{\text{pitch}}(\theta) &= \text{blkdiag}(\mathbf{R}_M, 1, \mathbf{R}_M^\circ) \mathbf{T}_M^{(1,3)}(\phi), \\ \mathbf{R}_{2M+1}^{\text{roll}}(\theta) &= \text{blkdiag}(1, \mathbf{R}_M, \mathbf{R}_M^\circ) \mathbf{T}_M^{(2,3)}(\phi). \end{aligned}$$

Theorem 1: Let $\phi \in C^1$ with $\phi(0) = 0$. Then $\mathbf{R}_N^{\text{axis}}(\theta)$ satisfies:

- 1) $\mathbf{R}_N^{\text{axis}}(\theta) \in SO(N)$;
- 2) $\mathbf{R}_N^{\text{axis}}(0) = \mathbf{I}_N$;

3) $\theta \mapsto \mathbf{R}_N^{\text{axis}}(\theta)$ is C^1 ;

4) For $N = 2^k$, the yaw/pitch/roll families remain distinct due to axis-dependent skew-symmetric exponential maps.

(Proof see Appendix B)

C. Definitions

Definition 1 (Type I AGFRFT): Given a graph signal $\mathbf{x} \in \mathbb{R}^N$, the type I AGFRFT (I-AGFRFT) associated with the angular parameter $\theta \in [0, 2\pi]$ and the fractional-order parameter $\alpha \in \mathbb{R}$ is defined by

$$\widehat{\mathbf{x}}_\theta^{\alpha, \text{I}} = \mathbf{F}_\theta^{\alpha, \text{I}} \mathbf{x}, \quad (21)$$

where $\mathbf{F}_\theta^{\alpha, \text{I}} = \mathbf{F}_\theta^\alpha$ denotes the transformation matrix.

Definition 2 (Type II AGFRFT): Let \mathbf{u}_k^α , $k = 1, 2, \dots, N$, denote the eigenvectors that are the columns of the unitary matrix $\mathbf{F}^{-\alpha}$. By rotating these eigenvectors using the rotation matrix $\mathbf{R}_N^{\text{axis}}(\theta)$, one obtains a unitary matrix

$$\mathbf{U}_{\theta, \alpha} = \mathbf{R}_N^{\text{axis}}(\theta) \mathbf{F}^{-\alpha}. \quad (22)$$

Then, the type II AGFRFT (II-AGFRFT) of the graph signal \mathbf{x} is defined as

$$\widehat{\mathbf{x}}_\theta^{\alpha, \text{II}} = \mathbf{F}_\theta^{\alpha, \text{II}} \mathbf{x}, \quad (23)$$

where $\mathbf{F}_\theta^{\alpha, \text{II}} = \mathbf{U}_{\theta, \alpha}^{-1} = \mathbf{U}_{\theta, \alpha}^H$.

D. Properties

This subsection presents several fundamental properties of I-AGFRFT and II-AGFRFT, together with rigorous proofs for each (Proof see Appendix C). For brevity, denote the original GFT matrix as $\mathbf{F} = \mathbf{U}^H$, the rotation matrix family as $\mathbf{R}_N^{\text{axis}}(\theta) \in SO(N)$, and the rotated basis as $\mathbf{U}_\theta = \mathbf{R}_N^{\text{axis}}(\theta) \mathbf{U}$, hence $\mathbf{F}_\theta = \mathbf{U}_\theta^H$. The fractional matrix power is defined as the matrix function $(\cdot)^\alpha$ via the principal branch of the matrix logarithm: $\mathbf{A}^\alpha := \exp(\alpha \log \mathbf{A})$ (valid when the spectrum avoids the branch cut of the logarithm or a continuous branch has been chosen).

Property 1 (Identity): When both the rotation angle and the fractional order are zero, both I- and II-type AGFRFT degenerate to the identity mapping: $\mathbf{F}_0^{0, \text{I}} = \mathbf{F}_0^{0, \text{II}} = \mathbf{I}_N$.

Property 2 (Reduction): When $\alpha = 1$, both I- and II-type AGFRFT reduce to AGFT: $\mathbf{F}_\theta^{1, \text{I}} = \mathbf{F}_\theta^{1, \text{II}} = \mathbf{F}_\theta$. When $\theta = 0$, both I- and II-type AGFRFT reduce to GFRFT: $\mathbf{F}_0^{\alpha, \text{I}} = \mathbf{F}_0^{\alpha, \text{II}} = \mathbf{F}^\alpha$.

Property 3 (Index additivity): For I-AGFRFT (fixed angle θ), fractional orders are additive: for any $\alpha_1, \alpha_2 \in \mathbb{R}$, assuming the logarithm branch is chosen consistently,

$$(\mathbf{F}_\theta)^{\alpha_1} (\mathbf{F}_\theta)^{\alpha_2} = (\mathbf{F}_\theta)^{\alpha_1 + \alpha_2}.$$

For II-AGFRFT, simple index additivity does not generally hold:

$$\begin{aligned} \mathbf{F}_\theta^{\alpha_1, \text{II}} \mathbf{F}_\theta^{\alpha_2, \text{II}} &= \mathbf{F}^{\alpha_1} \mathbf{R}_N^{\text{axis}}(\theta)^H \mathbf{F}^{\alpha_2} \mathbf{R}_N^{\text{axis}}(\theta)^H \\ &\neq \mathbf{F}^{\alpha_1 + \alpha_2} \mathbf{R}_N^{\text{axis}}(\theta)^H, \end{aligned}$$

unless the commutativity condition $\mathbf{R}_N^{\text{axis}}(\theta)^H \mathbf{F}^{\alpha_2} = \mathbf{F}^{\alpha_2} \mathbf{R}_N^{\text{axis}}(\theta)^H$ (equivalently $\mathbf{R}_N^{\text{axis}}(\theta) \mathbf{F}^{\alpha_2} = \mathbf{F}^{\alpha_2} \mathbf{R}_N^{\text{axis}}(\theta)$) is satisfied.

Algorithm 1 Grid Search for Optimal AGFRFT Filtering

```

1: Input:  $\mathbf{y}$ ,  $\mathbf{x}$ ,  $\mathbf{G}$ , AGFRFT type (I/II)
2: Parameters:  $\theta \subseteq [0, 2\pi]$ ,  $\alpha \subseteq [0, 1]$  (discretized grids),
    $\kappa = 1$ 
3: Output:  $(\theta^*, \alpha^*)$ ,  $\mathbf{H}^*$ 
4:  $\text{MSE}_{\min} \leftarrow +\infty$ ,  $\theta^* \leftarrow 0$ ,  $\alpha^* \leftarrow 0$ ,  $\mathbf{H}^* \leftarrow \mathbf{I}$ 
5: for each  $\theta$  do
6:   for each  $\alpha$  do
7:      $\mathbf{F}_{\theta, \alpha} \leftarrow$  AGFRFT matrix (Type I/II)
8:      $\mathbf{H} \leftarrow \mathbf{T}_{\theta, \alpha}^{-1} \mathbf{q}_{\theta, \alpha}$  (Eq. 25)
9:      $\tilde{\mathbf{x}} \leftarrow \mathbf{F}_{\theta, \alpha}^{-1} \mathbf{H} \mathbf{F}_{\theta, \alpha} \mathbf{y}$  (Eq. 24)
10:     $\text{MSE} \leftarrow \|\tilde{\mathbf{x}} - \mathbf{x}\|_2^2 / N$ 
11:    if  $\text{MSE} < \text{MSE}_{\min}$  then
12:       $\text{MSE}_{\min} \leftarrow \text{MSE}$ ,  $\theta^* \leftarrow \theta$ ,  $\alpha^* \leftarrow \alpha$ ,  $\mathbf{H}^* \leftarrow \mathbf{H}$ 
13:    end if
14:  end for
15: end for
16: return  $(\theta^*, \alpha^*, \mathbf{H}^*)$ 

```

Property 4 (Unitarity): With appropriate choice of logarithm branch, both I- and II-type AGFRFT are unitary operators, and energy preservation holds: $(\mathbf{F}_{\theta}^{\alpha, \text{I/II}})^{\text{H}} \mathbf{F}_{\theta}^{\alpha, \text{I/II}} = \mathbf{I}_N$.

Property 5 (Reversibility): Both I-AGFRFT and II-AGFRFT admit well-defined inverses. Concretely:

- **I-AGFRFT.** For any real α , $(\mathbf{F}_{\theta}^{\alpha, \text{I}})^{-1} = \mathbf{F}_{\theta}^{-\alpha, \text{I}}$, i.e. the inverse is obtained by negating the fractional order.
- **II-AGFRFT.** Let $\mathbf{U}_{\theta, \alpha} := \mathbf{R}_N^{\text{axis}}(\theta) \mathbf{F}^{-\alpha}$, $\mathbf{F}_{\theta}^{\alpha, \text{II}} = \mathbf{U}_{\theta, \alpha}^{\text{H}}$. Then the inverse of $\mathbf{F}_{\theta}^{\alpha, \text{II}}$ is the matrix $(\mathbf{F}_{\theta}^{\alpha, \text{II}})^{-1} = \mathbf{R}_N^{\text{axis}}(\theta) \mathbf{F}^{-\alpha}$. In particular, the operation “replace α by $-\alpha$ in the II-definition” (which yields $\mathbf{F}^{-\alpha} \mathbf{R}_N^{\text{axis}}(\theta)^{\text{H}}$) does *not* in general produce the inverse; equality holds only under the additional commutation condition $\mathbf{R}_N^{\text{axis}}(\theta)^{\text{H}} \mathbf{F}^{\beta} = \mathbf{F}^{\beta} \mathbf{R}_N^{\text{axis}}(\theta)^{\text{H}}$ for the relevant β .

IV. OPTIMAL ANGULAR GRAPH FRACTIONAL FOURIER FILTERING

Given observed signal $\mathbf{y} = \mathbf{G}\mathbf{x} + \mathbf{n}$, where $\mathbf{G} \in \mathbb{C}^{N \times N}$ is a known transformation, and \mathbf{n} denotes the noise. We define the AGFRFT Wiener filtering method. Specifically, the AGFRFT $_{\theta, \alpha}$ filtering formula reads:

$$\tilde{\mathbf{x}} = \mathbf{F}_{\theta, \alpha}^{-1} \mathbf{H} \mathbf{F}_{\theta, \alpha} \mathbf{y}, \quad (24)$$

where $\mathbf{F}_{\theta, \alpha} = \mathbf{F}_{\theta}^{\alpha, \text{I}}$ or $\mathbf{F}_{\theta}^{\alpha, \text{II}}$. When $\mathbf{F}_{\theta, \alpha} = \mathbf{F}_{\theta}^{\alpha, \text{I}}$, it corresponds the I-AGFRFT Wiener filtering method which simplifies as I-AGFRFT $_{\theta, \alpha}$. When $\mathbf{F}_{\theta, \alpha} = \mathbf{F}_{\theta}^{\alpha, \text{II}}$, it corresponds the II-AGFRFT Wiener filtering method which simplifies as II-AGFRFT $_{\theta, \alpha}$.

A. Grid Search

The optimal filter \mathbf{H}^* is determined by solving the following minimization problem

$$\mathbf{H}^* = \arg \min_{\mathbf{H}} \mathbb{E} \left\{ \left\| \mathbf{F}_{\theta, \alpha}^{-1} \mathbf{H} \mathbf{F}_{\theta, \alpha} \mathbf{y} - \mathbf{x} \right\|_2^2 \right\}. \quad (25)$$

Algorithm 2 Gradient Descent for AGFRFT Filtering

```

1: Input:  $\mathbf{y}$ ,  $\mathbf{x}$ ,  $\mathbf{G}$ , AGFRFT type (I/II)
2: Parameters:
   • Initial filter:  $\mathbf{H}^{(0)}$ 
   • Initial parameters:  $(\theta^{(0)}, \alpha^{(0)}, \kappa^{(0)})$ 
   • Hyperparameters:  $\eta > 0$ ,  $T_{\max}$ 
3: Output: Optimal  $(\theta^*, \alpha^*, \kappa^*)$  and  $\mathbf{H}^*$ 
4:  $\mathcal{L}_{\min} \leftarrow +\infty$ ,  $\theta^* \leftarrow \theta^{(0)}$ ,  $\alpha^* \leftarrow \alpha^{(0)}$ ,  $\kappa^* \leftarrow \kappa^{(0)}$ ,  $\mathbf{H}^* \leftarrow \mathbf{H}^{(0)}$ 
5: for  $t = 0$  to  $T_{\max} - 1$  do
6:    $\mathbf{F}^{(t)} \leftarrow$  AGFRFT matrix (Type I/II)
7:    $\tilde{\mathbf{x}}^{(t)} \leftarrow (\mathbf{F}^{(t)})^{-1} \mathbf{H}^{(t)} \mathbf{F}^{(t)} \mathbf{y}$ 
8:    $\mathcal{L}^{(t)} \leftarrow \|\tilde{\mathbf{x}}^{(t)} - \mathbf{x}\|_2^2$  (Eq. 28)
9:   if  $\mathcal{L}^{(t)} < \mathcal{L}_{\min}$  then
10:     $\mathcal{L}_{\min} \leftarrow \mathcal{L}^{(t)}$ ,  $\theta^* \leftarrow \theta^{(t)}$ ,  $\alpha^* \leftarrow \alpha^{(t)}$ ,  $\kappa^* \leftarrow \kappa^{(t)}$ ,  $\mathbf{H}^* \leftarrow \mathbf{H}^{(t)}$ 
11:   end if
12:   Compute gradients:
      $\nabla_{\mathbf{H}} \mathcal{L}^{(t)}$ ,  $\partial \mathcal{L}^{(t)} / \partial \theta$ ,  $\partial \mathcal{L}^{(t)} / \partial \alpha$ ,  $\partial \mathcal{L}^{(t)} / \partial \kappa$ 
13:   Update filter:  $\mathbf{H}^{(t+1)} \leftarrow \mathbf{H}^{(t)} - \eta \nabla_{\mathbf{H}} \mathcal{L}^{(t)}$ 
14:   Update parameters:  $(\theta^{(t+1)}, \alpha^{(t+1)}, \kappa^{(t+1)}) \leftarrow (\theta^{(t)}, \alpha^{(t)}, \kappa^{(t)}) - \eta (\partial \mathcal{L}^{(t)} / \partial \theta, \partial \mathcal{L}^{(t)} / \partial \alpha, \partial \mathcal{L}^{(t)} / \partial \kappa)$ 
15: end for
16: return  $(\theta^*, \alpha^*, \kappa^*)$ ,  $\mathbf{H}^*$ 

```

The optimal coefficient vector \mathbf{h}^* can be derived using the Wiener-Hopf equation: $\mathbf{T}_{\theta, \alpha} \mathbf{h}^* = \mathbf{q}_{\theta, \alpha}$, where $\mathbf{T}_{\theta, \alpha}$ is the autocorrelation matrix and $\mathbf{q}_{\theta, \alpha}$ is the cross-correlation vector [49]–[51]. Provided that $\mathbf{T}_{\theta, \alpha}$ is invertible, the closed-form solution is: $\mathbf{h}^* = \mathbf{T}_{\theta, \alpha}^{-1} \mathbf{q}_{\theta, \alpha}$.

To optimize the angular graph fractional Fourier spectrum, the parameters θ and α can be selected using a grid search to minimize the MSE of the filtered signal:

$$(\theta^*, \alpha^*) = \arg \min_{\theta, \alpha} \mathbb{E} \left\{ \|\tilde{\mathbf{x}}(\theta, \alpha) - \mathbf{x}\|_2^2 \right\}, \quad (26)$$

where $\tilde{\mathbf{x}}(\theta, \alpha) = \mathbf{F}_{\theta, \alpha}^{-1} \mathbf{H}^* \mathbf{F}_{\theta, \alpha} \mathbf{y}$. The specific implementation of this grid search process is detailed in Algorithm 1. In this case, the recursive construction of the rotation matrix employs the mapping $\phi(\theta) = \kappa\theta$. To preserve periodicity in grid search, we fix $\kappa = 1$.

B. Gradient Descent

Although grid search provides a direct method to determine (θ^*, α^*) , it suffers from high computational complexity. To address this, we reformulate the optimization as a differentiable problem and apply gradient descent. Specifically, we jointly optimize the filter coefficients \mathbf{H} and the angular graph fractional Fourier spectrum parameters (θ, α, κ) :

$$(\mathbf{H}^*; \theta^*, \alpha^*, \kappa^*) = \arg \min_{\mathbf{H}; \theta, \alpha, \kappa} \mathbb{E} \left\{ \left\| \mathbf{F}_{\theta, \alpha, \kappa}^{-1} \mathbf{H} \mathbf{F}_{\theta, \alpha, \kappa} \mathbf{y} - \mathbf{x} \right\|_2^2 \right\}. \quad (27)$$

a) *Differentiability.*: The key observation is that the mapping $\phi(\theta) = \kappa\theta$ is continuously differentiable in both θ and κ . The recursive construction of the rotation matrix

$\mathbf{R}_N^{\text{axis}}(\theta)$ involves only matrix multiplications and the matrix exponential $\exp(\phi\mathbf{J})$, which are differentiable with respect to their arguments. Consequently, the AGFRFT operator $\mathbf{F}_{\theta,\alpha,\kappa}$ is differentiable with respect to (θ, α, κ) .

b) *Gradient updates.*: Define the loss function

$$\mathcal{L}(\mathbf{H}, \theta, \alpha, \kappa) = \left\| \mathbf{F}_{\theta,\alpha,\kappa}^{-1} \mathbf{H} \mathbf{F}_{\theta,\alpha,\kappa} \mathbf{y} - \mathbf{x} \right\|_2^2. \quad (28)$$

Since \mathcal{L} is differentiable in \mathbf{H} , θ , α , and κ , we can update parameters iteratively via a unified learning rate $\eta > 0$:

$$\mathbf{H}^{(t+1)} = \mathbf{H}^{(t)} - \eta \nabla_{\mathbf{H}} \mathcal{L}, \quad (29)$$

$$\theta^{(t+1)} = \theta^{(t)} - \eta \frac{\partial \mathcal{L}}{\partial \theta}, \quad (30)$$

$$\alpha^{(t+1)} = \alpha^{(t)} - \eta \frac{\partial \mathcal{L}}{\partial \alpha}, \quad (31)$$

$$\kappa^{(t+1)} = \kappa^{(t)} - \eta \frac{\partial \mathcal{L}}{\partial \kappa}. \quad (32)$$

The iterative process of gradient descent is summarized in Algorithm 2. Therefore, the gradient descent algorithm provides a principled and efficient alternative to grid search, enabling the simultaneous optimization of the filter coefficients \mathbf{H} and the spectrum parameters (θ, α, κ) .

C. Complexity and Convergence Analysis

The computational complexity of the two optimization strategies scales with the signal dimension N where grid search achieves a total complexity of $O(N_\alpha N_\theta N^3)$ with N_α and N_θ denoting the grid points for fractional order α and rotation angle θ respectively. This strategy is feasible for small-scale signals with $N < 100$ but becomes intractable for high-dimensional data due to the cubic scaling with N . In contrast, gradient descent has a total complexity of $O(TN^3)$ where T ranges from 300 to 1000 iterations and it outperforms grid search for high-dimensional signals with $N > 500$ by 1–2 orders of magnitude as T is significantly smaller than the product of N_α and N_θ especially for fine grids. Regarding convergence, the loss function \mathcal{L} is twice continuously differentiable owing to the smooth dependence of AGFRFT on its parameters. For the filter coefficients \mathbf{H} , the optimization problem is strictly convex when (θ, α, κ) are fixed leading to linear convergence to the unique optimal \mathbf{H}^* . For the spectral parameters (θ, α, κ) , the optimization is non-convex but the bounded gradients of \mathcal{L} ensure convergence to a stationary point. The theoretical properties of AGFRFT, including unitarity and degeneracy, enhance the structural rationality of the parameter optimization space and alleviate perturbations caused by spurious local minima in the vicinity of the optimal parameter region, ensuring the converged stationary point possesses favorable stability and consistency. Overall, the joint optimization converges within 300–1000 iterations for most practical graph signal processing tasks.

V. NUMERICAL EXPERIMENTS

To validate the effectiveness and versatility of the proposed AGFRFT framework, we conduct comprehensive denoising experiments across three categories of tasks: real-world

time series data, natural image data and three-dimensional point clouds. In all experiments, the denoising performance is quantitatively assessed using peak signal-to-noise ratio (PSNR), structural similarity index (SSIM), and mean squared error (MSE). For parameter optimization, we adopt two complementary strategies. Specifically, for relatively small-scale time series data, the fractional orders are determined through an exhaustive grid search, while for high-dimensional signals such as images and point clouds, the parameters are optimized via gradient descent to improve computational tractability.

A. Real-Data Denoising

We evaluate the proposed AGFRFT method on three real-world temporal datasets with inherent graph structures: Sea Surface Temperature (SST), PM-25 Concentration, and COVID-19 Daily Confirmed Cases. Each dataset is constructed as a sequence graph where nodes correspond to daily observations. To capture local structural dependencies, we build k-nearest neighbor (k-NN) graphs with $k = 2$, $k = 5$, and $k = 10$. We inject additive Gaussian noise with standard deviations $\sigma = 0.5$, $\sigma = 1.0$, and $\sigma = 1.5$. Performance is evaluated at temporal checkpoints $t = 100$, $t = 200$, and $t = 300$. To minimize the denoised MSE, we optimize the fractional order α (ranging from 0.1 to 1.0 with a step of 0.1) and rotation angle θ (ranging from 0 to 2π with a step of 0.628) via grid search. Experimental results under all settings are summarized in TABLES II–IV, with key findings as follows.

On the SST dataset, AGFRFT degenerates to GFRFT or AGFT in most cases (with optimal α approaching 1 or $\theta = 0$), as the SST signal is smooth and requires only simple transformations. Even so, AGFRFT still achieves modest performance improvements: for example, with $k = 2$, $t = 100$ and $\sigma = 1.0$, II-AGFRFT $_{\mathbf{R}_{\text{yaw}}}$ yields an MSE of 3.23900, which is 51.6% lower than GFRFT (MSE = 6.69039) and 9.1% lower than AGFT $_{\mathbf{R}_{\text{yaw}}}$ (MSE = 3.56208). In contrast, AGFRFT shows significant advantages on the PM-25 and COVID-19 datasets. For PM-25 with $k = 5$, $\sigma = 1.5$, and $t = 200$, I-AGFRFT $_{\mathbf{R}_{\text{roll}}}$ achieves an MSE of 3.43771, which is 22.5% lower than GFRFT (MSE = 4.43702) and 13.8% lower than AGFT $_{\mathbf{R}_{\text{roll}}}$ (MSE = 3.97306). For COVID-19 with $\sigma = 0.5$, I-AGFRFT $_{\mathbf{R}_{\text{roll}}}$ delivers MSE values of 0.19049 ($k = 2$, $t = 100$), 0.1367 ($k = 5$, $t = 200$), and 0.20304 ($k = 10$, $t = 300$); compared to GFRFT (MSE = 0.23814 at $k = 5$), this represents a 42.6% reduction. Additionally, AGFRFT maintains stability as k varies: on COVID-19 data with $\sigma = 0.5$ and $t = 100$, its MSE decreases steadily from 0.19049 ($k = 2$) to 0.17947 ($k = 10$), demonstrating adaptability to different graph densities. Overall, leveraging the joint adjustment of fractional order and rotation angle, AGFRFT adaptively degenerates to avoid overparameterization for simple signals and accurately matches the spectral structure of complex signals, outperforming GFRFT and AGFT significantly.

B. Image Denoising

We further evaluate the proposed AGFRFT framework on the Set12 dataset, a widely recognized benchmark for

TABLE II: Denoising results on the SST dataset.

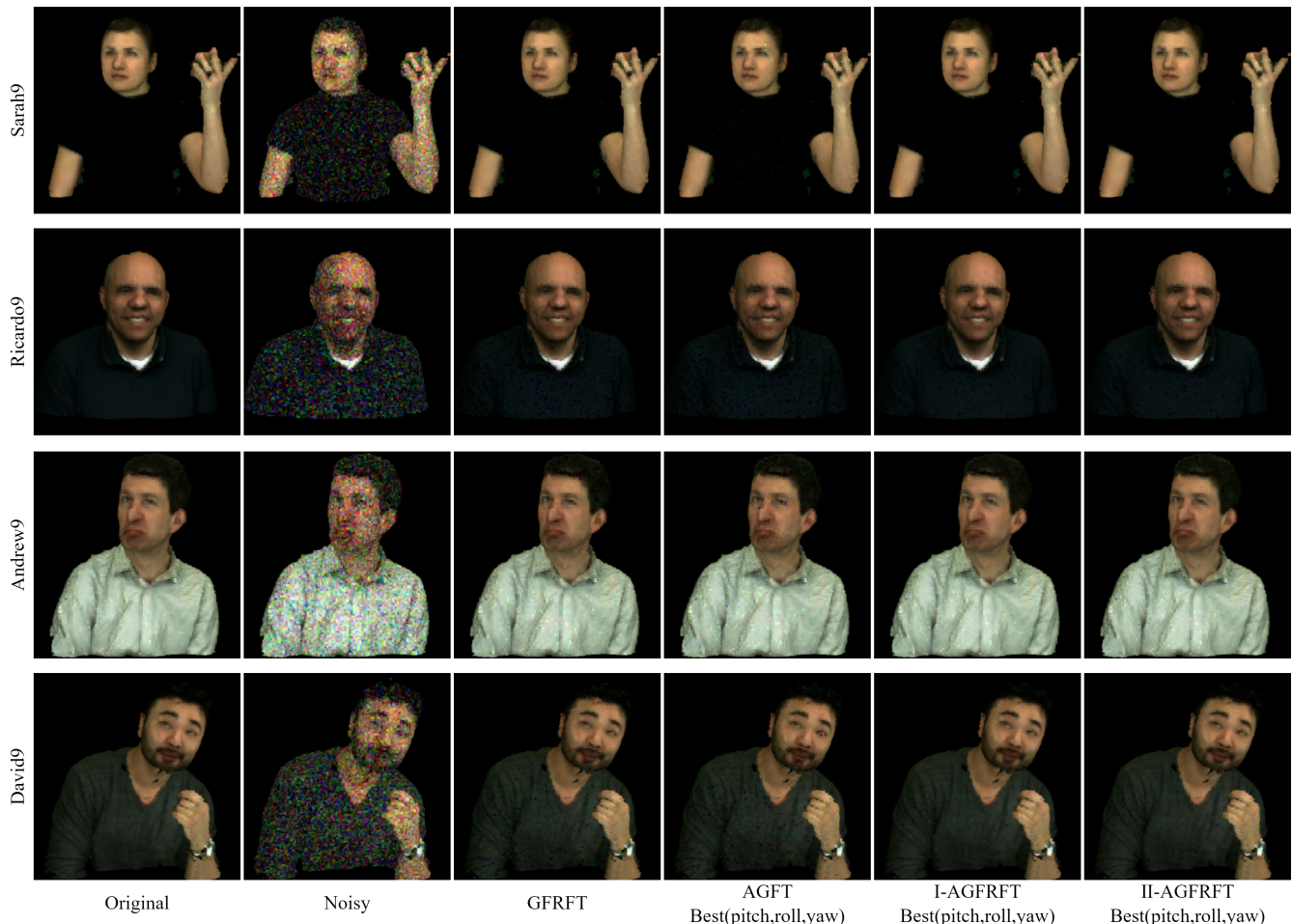
Method	2-NN			5-NN			10-NN		
	t=100	t=200	t=300	t=100	t=200	t=300	t=100	t=200	t=300
	$\sigma=0.5/1.0/1.5$	$\sigma=0.5/1.0/1.5$	$\sigma=0.5/1.0/1.5$	$\sigma=0.5/1.0/1.5$	$\sigma=0.5/1.0/1.5$	$\sigma=0.5/1.0/1.5$	$\sigma=0.5/1.0/1.5$	$\sigma=0.5/1.0/1.5$	$\sigma=0.5/1.0/1.5$
GFRFT	2.215806,690391/1.29184	1.710295,176349/08928	2.689417,150111/1.24275	0.59478/1.99083/3.94956	0.50694/1.65071/3.25967	0.62915/2.05859/3.98883	0.64382/2.01142/3.83035	0.75705/1.86447/3.41273	0.78842/2.12981/3.93222
(α)	(1.00/1.00/1.00)	(1.00/1.00/1.00)	(1.00/1.00/1.00)	(0.90/0.90/0.90)	(0.90/0.90/1.00)	(0.90/0.90/0.90)	(0.90/0.90/0.80)	(0.90/0.90/0.80)	(0.90/0.90/0.80)
AGFT _{R_{pitch}}	2.012695,043928/18926	1.710295,176348/90578	1.77664,869107/92144	0.73632,155144/04377	0.51522/1.67445/3.25967	0.90542/2.32151/4.12470	0.79375/2.47889/4.90941	0.80691/2.24334/4.27765	0.90688/2.60297/5.06552
(θ)	(2.513/2.513/2.513)	(6.283/6.283/6.283)	(2.513/2.513/2.513)	(0.000/0.000/6.283)	(0.000/0.000/0.000)	(0.000/0.000/6.283)	(6.283/6.283/6.283)	(6.283/6.283/6.283)	(6.283/6.283/6.283)
AGFT _{R_{roll}}	2.215805,683059/00940	1.710294,794827/78574	2.406635,517448/61191	0.73632,155144/04377	0.51522/1.67445/3.25967	0.90542/2.32151/4.12470	0.79375/2.47889/4.90941	0.80691/2.24334/4.27765	0.90688/2.60297/5.06552
(ϕ)	(0.000/3.770/3.770)	(0.000/5.027/5.027)	(3.770/3.770/3.770)	(0.000/0.000/0.000)	(0.000/0.000/0.000)	(0.000/0.000/0.000)	(0.000/0.000/0.000)	(0.000/0.000/0.000)	(0.000/0.000/0.000)
AGFT _{R_{yaw}}	1.078043,562086/57506	1.01939/3.366186/32097	1.19599/3.829306/6.88871	0.73632,155144/04377	0.51522/1.67445/3.25967	0.90542/2.32151/4.12470	0.79375/2.47889/4.90941	0.80691/2.24334/4.27765	0.90688/2.60297/5.06552
(θ)	(5.027/5.027/5.027)	(5.027/5.027/5.027)	(5.027/5.027/5.027)	(0.000/0.000/6.283)	(0.000/0.000/0.000)	(0.000/0.000/6.283)	(0.000/0.000/6.283)	(0.000/0.000/6.283)	(0.000/0.000/0.000)
I-AGFRFT _{R_{pitch}}	1.498414,040476/91580	1.710294,679017/70431	1.77664,478917/03622	0.59478/1.99083/3.94956	0.50694/1.65071/3.25967	0.62915/2.05859/3.98883	0.64382/2.01142/3.83035	0.75705/1.86447/3.41273	0.78842/2.12981/3.93222
(α)	(0.600,6.283/0.5)	(1.000,6.283/0.5)	(1.000,2.513/0.5)	(0.900,6.283/0.5)	(0.900,0.000/0.5)	(0.900,6.283/0.5)	(0.900,6.283/0.5)	(0.900,6.283/0.5)	(0.900,6.283/0.5)
(β)	(0.600,6.283/0.5)	(0.700,2.513/0.5)	(0.600,6.283/0.5)	(0.900,6.283/0.5)	(0.900,6.283/0.5)	(0.900,6.283/0.5)	(0.900,6.283/0.5)	(0.900,6.283/0.5)	(0.900,6.283/0.5)
(γ)	(0.600,6.283/0.5)	(0.600,6.283/0.5)	(0.600,6.283/0.5)	(0.900,6.283/0.5)	(0.900,6.283/0.5)	(0.900,6.283/0.5)	(0.900,6.283/0.5)	(0.900,6.283/0.5)	(0.900,6.283/0.5)
I-AGFRFT _{R_{roll}}	1.479734,542977/72341	1.482584,427617/25918	1.588184,225597/29859	0.59478/1.99083/3.94956	0.50694/1.65071/3.25967	0.62915/2.05859/3.98883	0.64382/2.01142/3.83035	0.75705/1.86447/3.41273	0.78842/2.12981/3.93222
(α)	(0.600,6.283/0.5)	(0.800,6.283/0.5)	(0.800,6.283/0.5)	(0.900,0.000/0.5)	(0.900,0.000/0.5)	(0.900,0.000/0.5)	(0.900,0.000/0.5)	(0.900,0.000/0.5)	(0.900,0.000/0.5)
(β)	(0.700,5.027/0.5)	(0.700,5.027/0.5)	(0.700,5.027/0.5)	(0.900,0.000/0.5)	(0.900,0.000/0.5)	(0.900,0.000/0.5)	(0.900,0.000/0.5)	(0.900,0.000/0.5)	(0.900,0.000/0.5)
(γ)	(0.700,5.027/0.5)	(0.900,5.027/0.5)	(0.900,5.027/0.5)	(0.900,0.000/0.5)	(0.900,0.000/0.5)	(0.900,0.000/0.5)	(0.900,0.000/0.5)	(0.900,0.000/0.5)	(0.900,0.000/0.5)
I-AGFRFT _{R_{yaw}}	1.078043,562086/57506	1.01939/3.366186/32097	1.19599/3.829306/6.88871	0.59478/1.99083/3.94956	0.50694/1.65071/3.25967	0.62915/2.05859/3.98883	0.64382/2.01142/3.83035	0.75705/1.86447/3.41273	0.78842/2.12981/3.93222
(α)	(1.000,5.027/0.5)	(1.000,5.027/0.5)	(1.000,5.027/0.5)	(0.900,0.000/0.5)	(0.900,6.283/0.5)	(0.900,0.000/0.5)	(0.900,0.000/0.5)	(0.900,0.000/0.5)	(0.900,0.000/0.5)
(β)	(1.000,5.027/0.5)	(1.000,5.027/0.5)	(1.000,5.027/0.5)	(0.900,0.000/0.5)	(1.000,0.000/0.5)	(0.900,6.283/0.5)	(0.800,6.283/0.5)	(0.800,6.283/0.5)	(0.800,6.283/0.5)
(γ)	(1.000,5.027/0.5)	(1.000,5.027/0.5)	(1.000,5.027/0.5)	(0.900,0.000/0.5)	(0.900,0.000/0.5)	(0.900,6.283/0.5)	(0.900,6.283/0.5)	(0.900,6.283/0.5)	(0.900,6.283/0.5)
II-AGFRFT _{R_{pitch}}	1.35057/0.68705/6.46863	1.22658/6.13436/43739	1.29856/3.59822/6.21617	0.59478/1.99083/3.94956	0.50694/1.65071/3.25967	0.62915/2.05859/3.98883	0.64382/2.01142/3.83035	0.75705/1.86447/3.41273	0.78842/2.12981/3.93222
(α)	(0.200,6.283/0.5)	(0.700,5.027/0.5)	(0.200,6.283/0.5)	(0.900,0.000/0.5)	(0.900,0.000/0.5)	(0.900,6.283/0.5)	(0.900,0.000/0.5)	(0.900,6.283/0.5)	(0.900,0.000/0.5)
(β)	(0.200,6.283/0.5)	(0.700,5.027/0.5)	(0.200,6.283/0.5)	(0.900,6.283/0.5)	(0.900,6.283/0.5)	(0.900,6.283/0.5)	(0.900,6.283/0.5)	(0.900,6.283/0.5)	(0.900,6.283/0.5)
(γ)	(0.200,6.283/0.5)	(0.700,5.027/0.5)	(0.200,6.283/0.5)	(0.900,6.283/0.5)	(0.900,6.283/0.5)	(0.900,6.283/0.5)	(0.900,6.283/0.5)	(0.900,6.283/0.5)	(0.900,6.283/0.5)
II-AGFRFT _{R_{roll}}	2.215805,172468/11764	1.710294,455036/99839	1.94084/8.26507/76223	0.59478/1.99083/3.94956	0.50694/1.65071/3.25967	0.62915/2.05859/3.98883	0.64382/2.01142/3.83035	0.75705/1.86447/3.41273	0.78842/2.12981/3.93222
(α)	(0.200,6.283/0.5)	(0.300,6.283/0.5)	(0.200,6.283/0.5)	(0.900,0.000/0.5)	(0.900,0.000/0.5)	(0.900,0.000/0.5)	(0.900,0.000/0.5)	(0.900,0.000/0.5)	(0.900,0.000/0.5)
(β)	(0.200,6.283/0.5)	(0.300,6.283/0.5)	(0.200,6.283/0.5)	(0.900,0.000/0.5)	(0.900,0.000/0.5)	(0.900,0.000/0.5)	(0.900,0.000/0.5)	(0.900,0.000/0.5)	(0.900,0.000/0.5)
(γ)	(0.200,6.283/0.5)	(0.300,6.283/0.5)	(0.200,6.283/0.5)	(0.900,0.000/0.5)	(0.900,0.000/0.5)	(0.900,0.000/0.5)	(0.900,0.000/0.5)	(0.900,0.000/0.5)	(0.900,0.000/0.5)
II-AGFRFT _{R_{yaw}}	1.078043,239005/90177	1.01939/3.366186/32317	1.17136/3.15399/5.72370	0.59478/1.99083/3.94956	0.50694/1.65071/3.25967	0.62915/2.05859/3.98883	0.64382/2.01142/3.83035	0.75705/1.86447/3.41273	0.78842/2.12981/3.93222
(α)	(0.900,5.655/0.5)	(1.000,5.027/0.5)	(0.900,5.655/0.5)	(0.900,6.283/0.5)	(0.900,6.283/0.5)	(0.900,0.000/0.5)	(0.900,0.000/0.5)	(0.900,6.283/0.5)	(0.900,6.283/0.5)
(β)	(0.900,5.655/0.5)	(1.000,5.027/0.5)	(0.900,5.655/0.5)	(0.900,0.000/0.5)	(0.900,0.000/0.5)	(0.900,0.000/0.5)	(0.900,0.000/0.5)	(0.900,6.283/0.5)	(0.900,6.283/0.5)
(γ)	(0.900,5.655/0.5)	(0.900,5.655/0.5)	(0.900,5.655/0.5)	(0.900,0.000/0.5)	(1.000,0.000/0.5)	(0.900,0.000/0.5)	(0.900,6.283/0.5)	(0.900,6.283/0.5)	(0.900,6.283/0.5)

TABLE III: Denoising results on the PM-25 dataset.

Method	2-NN			5-NN			10-NN		
	t=100	t=200	t=300	t=100	t=200	t=300	t=100	t=200	t=300
	$\sigma=0.5/1.0/1.5$	$\sigma=0.5/1.0/1.5$	$\sigma=0.5/1.0/1.5$	$\sigma=0.5/1.0/1.5$	$\sigma=0.5/1.0/1.5$	$\sigma=0.5/1.0/1.5$	$\sigma=0.5/1.0/1.5$	$\sigma=0.5/1.0/1.5$	$\sigma=0.5/1.0/1.5$
GFRFT	1.062772,592963/99297	1.514812,993744/05960	0.820552,085363/14133	0.835021,945643/11697	1.79828/3.38244/4.3702	1.41911/2.96390/4.04588	0.65679/1.59864/2.52349	0.913782/1.55633/2.1209	1.146422,585993/73528
(α)	(0.90/0.90/0.80)	(0.50/0.80/0.80)	(1.00/1.00/1.00)	(1.00/1.00/1.00)	(0.50/0.50/0.60)	(0.00/0.00/0.00)	(0.80/0.80/0.80)	(0.60/0.60/0.70)	(0.70/0.70/0.40)
AGFT _{R_{pitch}}	1.145157,218511/94580	1.214982,706203/35267	0.820552,085363/14133	0.835021,945643/11697	1.94847/2.71590/3.90198	1.19304/2.24503/3.12475	1.10393/2.12089/3.05541	1.319182,822984/06107	1.184652,477413/48134
(β)	(3.142/0.000/0.885)	(2.513/2.513/2.513)	(0.000/0.000/0.000)	(0.000/0.000/0.000)	(5.027/0.027/3.770)	(2.513/2.513/2.513)	(0.000/0.000/0.000)	(1.885/1.885/4.398)	(3.770/2.513/2.513)
AGFT _{R_{roll}}	1.232082,718514/07542	1.419292,574353/62740	0.820552,085363/14133	0.835021,945643/11697	1.03554/2.60373/97306	0.97381/2.10921/2.89071	1.10393/2.12089/3.05541	1.08082/2.18063/6.4054	1.23842,33842/34132
(θ)	(0.000/0.000/0.000)	(0.000/0.000/0.000)	(0.000/0.000/0.000)	(0.000/0.000/0.000)	(1.257/1.1/2.57/1.257)	(0.000/0.000/0.000)	(0.000/0.000/0.000)	(1.885/1.885/1.885)	(6.283/6.283/6.283)
AGFT _{R_{yaw}}	1.232082,718514/07542	1.323522,754673/91027	0.820552,085363/14133	0.835021,945643/11697	1.168652,538966/60636	1.10732,44406/3.16840	0.99891/2.12089/3.05541	1.161132,689634/01089	0.923871,99285/299215
(ϕ)	(0.6283/0.000/0.000)	(1.257/1.257/0.628)	(0.000/0.000/0.000)	(0.628/5.655/5.655)	(3.142/5.027/1.885)	(1.419/5.027/1.885)	(2.513/0.000/0.000)	(4.398/4.398/4.398)	(3.142/3.142/3.142)
I-AGFRFT _{R_{pitch}}	1.062772,516693/77586	0.85390/0.29213/1.4565	0.80825/1.81142/2.69476	0.835021,945643/11697	1.150192,43295/51819	0.89103/2.18751/3.12475	0.65679/1.59864/2.52349	0.913782/1.55633/2.1209	0.62321/60560/2.5872
(α)	(0.800,5.027/0.5)	(0.600,1.257/0.5)	(0.400,6.283/0.5)	(0.900,1.885/0.5)	(0.900,1.885/0.5)	(0.800,1.885/0.5)	(0.600,6.283/0.5)	(0.600,0.000/0.5)	(0.700,2.513/0.5)
(β)	(0.800,5.027/0.5)	(0.600,1.257/0.5)	(0.400,6.283/0.5)	(1.000,6.283/0.5)	(0.400,1.885/0.5)	(0.800,1.885/0.5)	(0.800,6.283/0.5)	(0.600,0.000/0.5)	(0.700,2.513/0.5)
(γ)	(0.800,5.027/0.5)	(0.600,1.257/0.5)	(0.400,6.283/0.5)	(1.000,6.283/0.5)	(0.400,1.885/0.5)	(0.800,1.885/0.5)	(0.800,6.283/0.5)	(0.600,0.000/0.5)	(0.700,2.513/0.5)
I-AGFRFT _{R_{roll}}	1.062772,410923/61885	1.106552,502533/53129	0.800232,019673/08957	0.835021,945643/11697	0.93759/2.25501/4.3771	0.63573/1.78107/75387	0.65679/1.59864/2.52349	0.84205/2.00613/2.1209	0.881362,14633/02735
(α)	(0.900,0.000/0.5)	(0.500,3.770/0.5)	(0.300,5.027/0.5)	(1.000,0.000/0.5)	(0.700,3.142/0.5)	(0.300,5.027/0.5)	(0.800,0.000/0.5)	(0.600,1.257/0.5)	(0.100,6.555/0.5)
(β)	(0.700,6.283/0.5)	(0.800,1.257/0.5)	(0.300,5.027/0.5)	(1.000,0.000/0.5)	(0.700,3.142/0.5)	(0.300,5.027/0.5)	(0.800,0.000/0.5)	(0.600,1.257/0.5)	(0.600,6.283/0.5)
(γ)	(0.700,6.283/0.5)	(0.800,1.257/0.5)	(0.300,5.027/0.5)	(1.000,0.000/0.5)	(0.700,3.142/0.5)	(0.300,5.027/0.5)	(0.800,0.000/0.5)	(0.700,0.000/0.5)	(0.600,6.283/0.5)
I-AGFRFT _{R_{yaw}}	1.062772,592963/99297	1.121192,425545/55226	0.809782/0.02104/2.99489	0.835021,945643/11697	1				

TABLE VI: Point cloud denoising results on Microsoft Voxelized dataset.

Method	Sarah9			Ricardo9			Andrew9			David9		
	$\sigma=20$	$\sigma=30$	$\sigma=40$									
	PSNR (MSE)											
GFRFT	41.727 (6.719e-05)	38.568 (1.391e-04)	36.415 (2.283e-04)	38.200 (1.513e-04)	36.244 (2.375e-04)	34.936 (3.209e-04)	37.580 (1.746e-04)	34.402 (3.629e-04)	32.461 (5.674e-04)	37.749 (1.679e-04)	35.166 (3.043e-04)	33.325 (4.650e-04)
AGFT _{Rpitch}	41.101 (7.761e-05)	38.067 (1.561e-04)	35.520 (2.805e-04)	37.415 (1.813e-04)	35.577 (2.769e-04)	34.240 (3.767e-04)	36.472 (2.253e-04)	33.602 (4.363e-04)	31.463 (7.140e-04)	36.545 (2.216e-04)	34.192 (3.809e-04)	32.706 (5.363e-04)
AGFT _{Rroll}	40.983 (7.975e-05)	37.786 (1.665e-04)	36.110 (2.449e-04)	37.604 (1.736e-04)	35.781 (2.642e-04)	34.652 (3.426e-04)	36.111 (2.448e-04)	33.604 (4.361e-04)	31.751 (6.682e-04)	36.719 (2.129e-04)	34.611 (3.458e-04)	32.906 (5.122e-04)
AGFT _{Ryaw}	40.934 (8.065e-05)	37.804 (1.638e-04)	35.565 (2.776e-04)	37.480 (1.786e-04)	35.638 (2.730e-04)	34.210 (3.793e-04)	36.454 (2.263e-04)	33.789 (4.179e-04)	31.494 (7.090e-04)	36.626 (2.175e-04)	34.234 (3.772e-04)	32.602 (5.492e-04)
I-AGFRFT _{Rpitch}	46.455 (2.262e-05)	43.480 (4.488e-05)	41.283 (7.442e-05)	42.442 (5.699e-05)	40.416 (9.086e-05)	39.488 (1.125e-04)	42.789 (5.262e-05)	39.519 (1.117e-04)	37.308 (1.859e-04)	42.151 (6.094e-05)	39.877 (1.029e-04)	37.929 (1.611e-04)
I-AGFRFT _{Rroll}	46.043 (2.487e-05)	42.826 (5.217e-05)	40.834 (8.253e-05)	42.037 (6.256e-05)	40.463 (8.989e-05)	39.222 (1.196e-04)	42.453 (5.685e-05)	39.150 (1.216e-04)	36.790 (2.094e-04)	42.090 (6.180e-05)	39.728 (1.065e-04)	37.885 (1.627e-04)
I-AGFRFT _{Ryaw}	46.721 (2.127e-05)	43.764 (4.204e-05)	41.247 (7.503e-05)	42.247 (5.960e-05)	40.484 (8.945e-05)	39.424 (1.142e-04)	42.666 (5.412e-05)	39.517 (1.118e-04)	37.076 (1.961e-04)	42.448 (5.691e-05)	39.986 (1.003e-04)	38.175 (1.522e-04)
II-AGFRFT _{Rpitch}	46.436 (2.272e-05)	43.625 (4.340e-05)	41.392 (7.258e-05)	42.540 (5.571e-05)	40.548 (8.814e-05)	39.553 (1.109e-04)	42.841 (5.198e-05)	39.620 (1.091e-04)	37.491 (1.782e-04)	42.278 (5.919e-05)	39.997 (1.001e-04)	38.275 (1.488e-04)
II-AGFRFT _{Rroll}	46.110 (2.449e-05)	43.018 (4.991e-05)	41.374 (7.288e-05)	41.979 (6.340e-05)	40.542 (8.826e-05)	39.377 (1.154e-04)	42.524 (5.592e-05)	39.175 (1.209e-04)	36.979 (2.005e-04)	42.174 (6.061e-05)	39.896 (1.024e-04)	38.042 (1.570e-04)
II-AGFRFT _{Ryaw}	46.710 (2.133e-05)	43.911 (4.064e-05)	41.354 (7.321e-05)	42.309 (5.876e-05)	40.624 (8.662e-05)	39.619 (1.092e-04)	42.727 (5.337e-05)	39.392 (1.150e-04)	37.238 (1.889e-04)	42.475 (5.656e-05)	40.297 (9.338e-05)	38.454 (1.428e-04)

Fig. 3: Denoising results on *Sarah9*, *Ricardo9*, *Andrew9*, and *David9* ($\sigma = 40$). Columns: Original, Noisy, GFRFT, AGFT, I-AGFRFT, II-AGFRFT.

SSIM of 0.9980, significantly exceeding GFRFT (46.449 dB, $2.265e-05$, 0.9915) and the best-performing AGFT variant (AGFT with yaw rotation: 39.617 dB, $1.092e-04$, 0.9633). Even at a higher noise level ($\sigma = 40$), II-AGFRFT with roll rotation maintains superior performance on Peppers, achieving a PSNR of 47.611 dB compared to 42.217 dB of GFRFT, demonstrating its ability to suppress strong noise without over-smoothing while preserving structural details. The qualitative denoising results presented in Fig. 2 further validate these findings, where GFRFT fails to fully eliminate higher noise level ($\sigma = 40$) in texture-rich regions (e.g., Peppers' surfaces) and AGFT introduces noticeable blurring due to its defective degeneracy. In contrast, both I-AGFRFT and II-AGFRFT retain fine image details such as Starfish spines and Monarch

wing patterns while effectively removing noise, underscoring AGFRFT's practical effectiveness derived from a rigorous theoretical framework.

C. Point Cloud Denoising

To validate AGFRFT's effectiveness for high-dimensional geometric data, we evaluate its denoising performance on 3D point clouds using the Microsoft Voxelized Dataset3 [53], consistent with cross-task experimental protocols. Additive Gaussian noise with standard deviations $\sigma = 20$, $\sigma = 30$, and $\sigma = 40$ is injected into clean point clouds to simulate low-, medium-, and high-noise environments. Each point cloud is partitioned into local patches (up to 100 vertices per patch). For each patch, 10-nearest neighbor (10-NN)

graphs are constructed to model geometric dependencies: neighbors are identified via a k-d tree, edges are weighted using distance-based Gaussian kernels to emphasize proximity. Due to the high dimensionality and irregular topology of point cloud data, grid search is computationally infeasible. Instead, the fractional order α and rotation angle θ are optimized via gradient descent (learning rate = 0.01, 1000 epochs) to minimize MSE, with initial parameters set to correspond to GFT for theoretical consistency.

TABLE VI presents the quantitative denoising performance across all point cloud datasets. Both I-AGFRFT and II-AGFRFT (under pitch, roll, and yaw rotations) consistently outperform GFRFT and AGFT under all tested noise levels. In high-noise conditions ($\sigma = 40$), II-AGFRFT $_{\mathbf{R}_{\text{yaw}}}$ achieves the highest performance on *David9*, yielding a PSNR of 38.454 dB and an MSE of 1.428e-04. This represents a 5.13 dB improvement in PSNR and a 69.3% reduction in MSE compared with GFRFT (33.325 dB, 4.650e-04), and surpasses the best AGFT variant (AGFT $_{\mathbf{R}_{\text{roll}}}$, 32.906 dB, 5.122e-04) by 5.55 dB and 72.1%, respectively. Similarly, on *Andrew9*, II-AGFRFT $_{\mathbf{R}_{\text{pitch}}}$ attains a PSNR of 37.491 dB and an MSE of 1.782e-04, outperforming GFRFT (32.461 dB, 5.674e-04) by 5.03 dB in PSNR and 68.6% in MSE reduction. Under moderate noise conditions ($\sigma = 20$), AGFRFT remains superior, demonstrating robust denoising capability even in less noisy environments. For *Sarah9*, I-AGFRFT $_{\mathbf{R}_{\text{yaw}}}$ achieves a PSNR of 46.721 dB and an MSE of 2.127e-05, improving upon GFRFT (41.727 dB, 6.719e-05) by 4.99 dB in PSNR and 68.3% in MSE reduction. Likewise, *Ricardo9* reaches its optimal performance with II-AGFRFT $_{\mathbf{R}_{\text{pitch}}}$ (PSNR = 42.540 dB, MSE = 5.571e-05), outperforming GFRFT (38.200 dB, 1.513e-04) by 4.34 dB in PSNR and 63.2% in MSE reduction. Fig. 3 shows that AGFRFT can effectively preserve the subtle features of point cloud signal values while suppressing noise, which is consistent with the lower MSE and higher PSNR observed in the quantitative results. This performance benefits from the joint optimization of the fractional order α and rotation angle θ , which enables better matching with the spectral structure of point cloud signals and provides valuable support for the denoising of 3D point cloud signals.

D. Discussion

Across the three categories of denoising experiments, namely real-world time series data, natural image data, and 3D point clouds, the proposed AGFRFT framework consistently demonstrates robust performance. To balance accuracy and scalability, we adopted differentiated parameter optimization strategies: grid search was used for small-scale time series data to identify stable parameter configurations, while gradient-based optimization was applied to high-dimensional images and 3D point clouds to ensure computational efficiency. This differentiated approach enables AGFRFT to achieve superior trade-offs between noise suppression and the preservation of structure or signal features across all tasks. It also confirms the framework's strong adaptability to diverse data modalities, ranging from temporal sequences to visual and geometric

graph signals, which highlights AGFRFT's versatility and robustness as a general framework for graph signal denoising.

VI. CONCLUSIONS

This study proposes a novel AGFRFT framework to address the core limitations of existing graph spectral transformation methods, namely, the lack of angular control in the GFRFT and the inconsistency in the theoretical degeneracy of the AGFT. To achieve this goal, the framework fundamentally resolves AGFT's theoretical inconsistency of AGFT by recursively constructing a degeneracy-friendly rotation matrix family. Based on this, two AGFRFT variants (I-AGFRFT and II-AGFRFT) are designed, with strict theoretical proofs completed to validate their core properties. A joint learnable parameterization strategy integrating fractional order α and rotation angle θ is simultaneously introduced to realize adaptive alignment with the structural characteristics of diverse graph signals. For the optimization of signals with different scales, the AGFRFT adopts a differentiated parameter optimization scheme: a grid search is selected for small-scale temporal signals to ensure parameter reliability, whereas gradient descent is employed for high-dimensional signals to balance efficiency and performance. Multimodal experiments fully confirm the comprehensive superiority of AGFRFT. In future work, we will focus on several directions: extending AGFRFT to dynamic graph signal processing, deeply integrating with GNNs to boost spectral feature extraction, optimizing computational efficiency for large-scale scenarios, and expanding to multi-task processing to enhance cross-field practical value.

APPENDIX A

PROOF OF ORTHOGONALITY PRESERVATION

Let \mathbf{J} be a skew-symmetric matrix and ϕ an arbitrary scalar. A fundamental property of the matrix exponential states that the transpose of the exponential is the exponential of the transposed matrix, giving $(\exp(\phi\mathbf{J}))^\top = \exp((\phi\mathbf{J})^\top)$. Substituting the skew-symmetry of \mathbf{J} ($\mathbf{J}^\top = -\mathbf{J}$), we obtain $(\exp(\phi\mathbf{J}))^\top = \exp(-\phi\mathbf{J})$. Since $\phi\mathbf{J}$ and $-\phi\mathbf{J}$ commute (i.e., $(\phi\mathbf{J})(-\phi\mathbf{J}) = (-\phi\mathbf{J})(\phi\mathbf{J})$), the product of their exponentials satisfies $\exp(-\phi\mathbf{J})\exp(\phi\mathbf{J}) = \exp(-\phi\mathbf{J} + \phi\mathbf{J}) = \exp(\mathbf{0}) = \mathbf{I}$, where \mathbf{I} is the identity matrix. This confirms $\exp(\phi\mathbf{J})^\top \exp(\phi\mathbf{J}) = \mathbf{I}$, the defining condition for an orthogonal matrix. Thus, $\exp(\phi\mathbf{J})$ is orthogonal. \square

APPENDIX B

PROOF OF THEOREM 1

Induction on N . Base cases $N = 1, 2, 3$ are immediate. Assume the theorem holds for M , i.e., $\mathbf{R}_M, \mathbf{R}_M^\circ \in SO(M)$, block rotations belong to $SO(2M)$ (or $SO(2M + 1)$), and $\exp(\phi\mathbf{J}_{\text{axis}}) \in SO(2M)$. For the inductive step, products of matrices in $SO(\cdot)$ preserve orthogonality and determinant 1, hence remain in $SO(N)$. At $\theta = 0$, $\mathbf{R}_N^{\text{axis}}(0)$ reduces to the identity matrix by construction. Differentiability follows from composition of C^1 maps (matrix exponential and $\phi(\theta) \in C^1$). Axis distinction is guaranteed by the design of \mathbf{J}_{axis} matrices, which maintain unique sparsity patterns for yaw/pitch/roll families. Thus, all four properties are satisfied. \square

APPENDIX C

PROOFS OF AGFRFT FUNDAMENTAL PROPERTIES

Proof of Property 1 (Identity): Since $\mathbf{R}_N^{\text{axis}}(0) = \mathbf{I}_N$ (degeneracy of the rotation family) and $\mathbf{F}^0 = \mathbf{I}_N$ (the zero power of any matrix is the identity), we have

$$\mathbf{F}_0^{\alpha, \text{I}} = (\mathbf{F}_0)^0 = \mathbf{I}_N, \quad \mathbf{F}_0^{\alpha, \text{II}} = \mathbf{F}^0 \mathbf{R}_N^{\text{axis}}(0)^{\text{H}} = \mathbf{I}_N. \quad \square$$

Proof of Property 2 (Reduction): For $\alpha = 1$, $\mathbf{F}_\theta^{1, \text{I}} = (\mathbf{F}_\theta)^1 = \mathbf{F}_\theta$, while for type II, $\mathbf{F}_\theta^{1, \text{II}} = \mathbf{F}^1 \mathbf{R}_N^{\text{axis}}(\theta)^{\text{H}} = \mathbf{F} \mathbf{R}_N^{\text{axis}}(\theta)^{\text{H}} = \mathbf{F}_\theta$. Note that $\mathbf{F}_\theta = \mathbf{U}_\theta^{\text{H}} = (\mathbf{R}_N^{\text{axis}}(\theta) \mathbf{U})^{\text{H}} = \mathbf{U}^{\text{H}} \mathbf{R}_N^{\text{axis}}(\theta)^{\text{H}} = \mathbf{F} \mathbf{R}_N^{\text{axis}}(\theta)^{\text{H}}$, so the above is equivalent to \mathbf{F}_θ . When $\theta = 0$, $\mathbf{R}_N^{\text{axis}}(0) = \mathbf{I}_N$, hence $\mathbf{F}_0 = \mathbf{F}$, giving $\mathbf{F}_0^{\alpha, \text{I}} = (\mathbf{F}_0)^\alpha = \mathbf{F}^\alpha$, $\mathbf{F}_0^{\alpha, \text{II}} = \mathbf{F}^\alpha \mathbf{R}_N^{\text{axis}}(0)^{\text{H}} = \mathbf{F}^\alpha$. \square

Proof of Property 3 (Index additivity): Type I: By the definition of matrix functions, fixing \mathbf{F}_θ and a chosen $\log \mathbf{F}_\theta$,

$$\begin{aligned} (\mathbf{F}_\theta)^{\alpha_1} (\mathbf{F}_\theta)^{\alpha_2} &= \exp(\alpha_1 \log \mathbf{F}_\theta) \exp(\alpha_2 \log \mathbf{F}_\theta) \\ &= \exp((\alpha_1 + \alpha_2) \log \mathbf{F}_\theta) \\ &= (\mathbf{F}_\theta)^{\alpha_1 + \alpha_2}, \end{aligned}$$

where the product combines because the logarithm matrices are identical. Type II: By direct substitution,

$$\mathbf{F}_\theta^{\alpha_1, \text{II}} \mathbf{F}_\theta^{\alpha_2, \text{II}} = \mathbf{F}^{\alpha_1} \mathbf{R}^{\text{H}} \mathbf{F}^{\alpha_2} \mathbf{R}^{\text{H}} = \mathbf{F}^{\alpha_1} (\mathbf{R}^{\text{H}} \mathbf{F}^{\alpha_2} \mathbf{R}^{\text{H}}),$$

and since \mathbf{R}^{H} and \mathbf{F}^{α_2} do not generally commute, the expression cannot be reduced to $\mathbf{F}^{\alpha_1 + \alpha_2} \mathbf{R}^{\text{H}}$, except under the commutativity condition. \square

Proof of Property 4 (Unitarity): For type II: \mathbf{F}^α is a unitary matrix function of \mathbf{F} (since \mathbf{F} itself is unitary, $z \mapsto z^\alpha$ maps the unit circle to itself, and $\log \mathbf{F}$ is skew-Hermitian), hence \mathbf{F}^α is unitary; $\mathbf{R}_N^{\text{axis}}(\theta) \in SO(N) \subset U(N)$, thus $\mathbf{R}_N^{\text{axis}}(\theta)^{\text{H}}$ is also unitary. Their product $\mathbf{F}^\alpha \mathbf{R}^{\text{H}}$ is a product of unitary matrices, hence unitary. For type I: \mathbf{F}_θ is unitary, so $(\mathbf{F}_\theta)^\alpha$ is also unitary (via $\exp(\alpha \log \mathbf{F}_\theta)$ with $\log \mathbf{F}_\theta$ skew-Hermitian). \square

Proof of Property 5 (Reversibility): **I-AGFRFT.** By definition $\mathbf{F}_\theta^{\alpha, \text{I}} = (\mathbf{F}_\theta)^\alpha$ where the matrix power is taken via the principal matrix logarithm:

$$(\mathbf{F}_\theta)^\alpha = \exp(\alpha \log \mathbf{F}_\theta).$$

Therefore

$$\begin{aligned} (\mathbf{F}_\theta)^\alpha (\mathbf{F}_\theta)^{-\alpha} &= \exp(\alpha \log \mathbf{F}_\theta) \exp(-\alpha \log \mathbf{F}_\theta) \\ &= \exp(0) = \mathbf{I}_N, \end{aligned}$$

and similarly for the reverse order. Hence $(\mathbf{F}_\theta)^{-\alpha}$ is the inverse of $(\mathbf{F}_\theta)^\alpha$.

II-AGFRFT. By construction

$$\begin{aligned} \mathbf{F}_\theta^{\alpha, \text{II}} &= \mathbf{U}_{\theta, \alpha}^{\text{H}} = (\mathbf{R}_N^{\text{axis}}(\theta) \mathbf{F}^{-\alpha})^{\text{H}} \\ &= (\mathbf{F}^{-\alpha})^{\text{H}} \mathbf{R}_N^{\text{axis}}(\theta)^{\text{H}} = \mathbf{F}^\alpha \mathbf{R}_N^{\text{axis}}(\theta)^{\text{H}}, \end{aligned}$$

where we used unitarity of \mathbf{F} to get $(\mathbf{F}^{-\alpha})^{\text{H}} = \mathbf{F}^\alpha$. Consider the candidate inverse

$$\mathbf{V} := \mathbf{R}_N^{\text{axis}}(\theta) \mathbf{F}^{-\alpha}.$$

We verify it is both a right- and left-inverse. First the right product:

$$\begin{aligned} \mathbf{F}_\theta^{\alpha, \text{II}} \mathbf{V} &= (\mathbf{F}^\alpha \mathbf{R}_N^{\text{axis}}(\theta)^{\text{H}}) (\mathbf{R}_N^{\text{axis}}(\theta) \mathbf{F}^{-\alpha}) \\ &= \mathbf{F}^\alpha (\mathbf{R}_N^{\text{axis}}(\theta)^{\text{H}} \mathbf{R}_N^{\text{axis}}(\theta)) \mathbf{F}^{-\alpha} = \mathbf{F}^\alpha \mathbf{I}_N \mathbf{F}^{-\alpha} = \mathbf{I}_N, \end{aligned}$$

since $\mathbf{R}_N^{\text{axis}}(\theta) \in SO(N) \subset U(N)$ implies $\mathbf{R}_N^{\text{axis}}(\theta)^{\text{H}} \mathbf{R}_N^{\text{axis}}(\theta) = \mathbf{I}_N$, and $\mathbf{F}^\alpha \mathbf{F}^{-\alpha} = \mathbf{I}_N$. Next the left product:

$$\begin{aligned} \mathbf{V} \mathbf{F}_\theta^{\alpha, \text{II}} &= (\mathbf{R}_N^{\text{axis}}(\theta) \mathbf{F}^{-\alpha}) (\mathbf{F}^\alpha \mathbf{R}_N^{\text{axis}}(\theta)^{\text{H}}) \\ &= \mathbf{R}_N^{\text{axis}}(\theta) (\mathbf{F}^{-\alpha} \mathbf{F}^\alpha) \mathbf{R}_N^{\text{axis}}(\theta)^{\text{H}} \\ &= \mathbf{R}_N^{\text{axis}}(\theta) \mathbf{I}_N \mathbf{R}_N^{\text{axis}}(\theta)^{\text{H}} = \mathbf{I}_N. \end{aligned}$$

Thus \mathbf{V} is the two-sided inverse of $\mathbf{F}_\theta^{\alpha, \text{II}}$ and we obtain

$$(\mathbf{F}_\theta^{\alpha, \text{II}})^{-1} = \mathbf{R}_N^{\text{axis}}(\theta) \mathbf{F}^{-\alpha}.$$

Why $\mathbf{F}^{-\alpha} \mathbf{R}_N^{\text{axis}}(\theta)^{\text{H}}$ is not generally the inverse. The matrix obtained by substituting $\alpha \mapsto -\alpha$ into the II-definition is $\mathbf{F}^{-\alpha} \mathbf{R}_N^{\text{axis}}(\theta)^{\text{H}}$. Its product with $\mathbf{F}_\theta^{\alpha, \text{II}} = \mathbf{F}^\alpha \mathbf{R}_N^{\text{axis}}(\theta)^{\text{H}}$ yields

$$\begin{aligned} &(\mathbf{F}^\alpha \mathbf{R}_N^{\text{axis}}(\theta)^{\text{H}}) (\mathbf{F}^{-\alpha} \mathbf{R}_N^{\text{axis}}(\theta)^{\text{H}}) \\ &= \mathbf{F}^\alpha (\mathbf{R}_N^{\text{axis}}(\theta)^{\text{H}} \mathbf{F}^{-\alpha}) \mathbf{R}_N^{\text{axis}}(\theta)^{\text{H}}, \end{aligned}$$

which does not simplify to \mathbf{I}_N in general because $\mathbf{R}_N^{\text{axis}}(\theta)^{\text{H}}$ and $\mathbf{F}^{-\alpha}$ need not commute. Equality would hold only if the commutation $\mathbf{R}_N^{\text{axis}}(\theta)^{\text{H}} \mathbf{F}^{-\alpha} = \mathbf{F}^{-\alpha} \mathbf{R}_N^{\text{axis}}(\theta)^{\text{H}}$ is satisfied, in which case the two candidate inverses coincide. \square

REFERENCES

- [1] A. Sandryhaila and J. M. Moura, "Discrete signal processing on graphs," *IEEE Trans. Signal Process.*, vol. 61, no. 7, pp. 1644–1656, Apr. 2013.
- [2] X. Song, L. Chai, and J. Zhang, "Graph signal processing approach to qsar/qspr model learning of compounds," *IEEE Trans. Pattern Anal. Mach. Intell.*, vol. 44, no. 4, pp. 1963–1973, Apr. 2020.
- [3] A. Ortega, P. Frossard, J. Kovačević, J. M. Moura, and P. Vandergheynst, "Graph signal processing: Overview, challenges, and applications," *Proc. IEEE*, vol. 106, no. 5, pp. 808–828, May 2018.
- [4] A. Sandryhaila and J. M. Moura, "Big data analysis with signal processing on graphs: Representation and processing of massive data sets with irregular structure," *IEEE Signal Process. Mag.*, vol. 31, no. 5, pp. 80–90, Sep. 2014.
- [5] L. Stankovic, D. Mandic, M. Dakovic, M. Brajovic, B. Scalzo, and T. Constantinides, "Graph signal processing—part i: Graphs, graph spectra, and spectral clustering," *arXiv preprint arXiv:1907.03467*, 2019.
- [6] L. Stankovic, D. Mandic, M. Dakovic, M. Brajovic, B. Scalzo, and A. G. Constantinides, "Graph signal processing—part ii: Processing and analyzing signals on graphs," *arXiv preprint arXiv:1909.10325*, 2019.
- [7] R. Li, X. Yuan, M. Radfar, P. Marendy, W. Ni, T. J. O'Brien, and P. M. Casillas-Espinosa, "Graph signal processing, graph neural network and graph learning on biological data: A systematic review," *IEEE Rev. Biomed. Eng.*, vol. 16, pp. 109–135, 2021.
- [8] G. Leus, A. G. Marques, J. M. Moura, A. Ortega, and D. I. Shuman, "Graph signal processing: History, development, impact, and outlook," *IEEE Signal Process. Mag.*, vol. 40, no. 4, pp. 49–60, Jul. 2023.
- [9] E. Isufi, F. Gama, D. I. Shuman, and S. Segarra, "Graph filters for signal processing and machine learning on graphs," *IEEE Trans. Signal Process.*, vol. 72, pp. 4745–4781, 2024.
- [10] L. Stanković, D. Mandić, M. Daković, B. Scalzo, M. Brajović, E. Sejdić, and A. G. Constantinides, "Vertex-frequency graph signal processing: A comprehensive review," *Digit. Signal Process.*, vol. 107, p. 102802, 2020.
- [11] D. Thanou, D. I. Shuman, and P. Frossard, "Learning parametric dictionaries for signals on graphs," *IEEE Trans. Signal Process.*, vol. 62, no. 15, pp. 3849–3862, 2014.
- [12] S. Chen, R. Varma, A. Singh, and J. Kovačević, "Signal representations on graphs: Tools and applications," *arXiv preprint arXiv:1512.05406*, 2015.

- [13] X. Pei, X. Deng, N. N. Xiong, S. Mumtaz, and J. Wu, "Complex graph analysis and representation learning: Problems, techniques, and applications," *IEEE Trans. Netw. Sci. Eng.*, vol. 11, no. 5, pp. 4990–5007, 2024.
- [14] G. Cheung, E. Magli, Y. Tanaka, and M. K. Ng, "Graph spectral image processing," *Proc. IEEE*, vol. 106, no. 5, pp. 907–930, May 2018.
- [15] A. Ortega, *Introduction to Graph Signal Processing*. Cambridge Univ. Press, 2022.
- [16] B. Girault, P. Gonçalves, and É. Fleury, "Translation on graphs: An isometric shift operator," *IEEE Signal Process. Lett.*, vol. 22, no. 12, pp. 2416–2420, Dec. 2015.
- [17] S. Chen, F. Cerda, P. Rizzo, J. Bielik, J. H. Garrett, and J. Kovačević, "Semi-supervised multiresolution classification using adaptive graph filtering with application to indirect bridge structural health monitoring," *IEEE Trans. Signal Process.*, vol. 62, no. 11, pp. 2879–2893, Jun. 2014.
- [18] L. Dabush and T. Routtenberg, "Verifying the smoothness of graph signals: A graph signal processing approach," *IEEE Trans. Signal Process.*, 2024.
- [19] K. Lu and A. Ortega, "Fast graph Fourier transforms based on graph symmetry and bipartition," *IEEE Trans. Signal Process.*, vol. 67, no. 18, pp. 4855–4869, Sep. 2019.
- [20] F. R. K. Chung, *Spectral Graph Theory*. Amer. Math. Soc., 1997, vol. 92.
- [21] D. Emms, E. R. Hancock, S. Severini, and R. C. Wilson, "A matrix representation of graphs and its spectrum as a graph invariant," *Electron. J. Combin.*, vol. 13, no. 1, pp. 1–14, 2006.
- [22] D. Cvetković, P. Rowlinson, and S. K. Simić, "Signless Laplacians of finite graphs," *Linear Algebra Appl.*, vol. 423, no. 1, pp. 155–171, 2007.
- [23] A. H. Ghodrati and M. A. Hosseinzadeh, "Signless Laplacian spectrum of a graph," *Linear Algebra Appl.*, vol. 682, pp. 257–267, 2024.
- [24] F. Ji, W. P. Tay, and A. Ortega, "Graph signal processing over a probability space of shift operators," *IEEE Trans. Signal Process.*, vol. 71, pp. 1159–1174, 2023.
- [25] F. Zhao and Z. Zhang, "Fractional graph spectral filtering based on unified graph representation matrix," *IEEE Signal Process. Lett.*, 2025.
- [26] D. I. Shuman, S. K. Narang, P. Frossard, A. Ortega, and P. Vandergheynst, "The emerging field of signal processing on graphs: Extending high-dimensional data analysis to networks and other irregular domains," *IEEE Signal Process. Mag.*, vol. 30, no. 3, pp. 83–98, May 2013.
- [27] A. Sandryhaila and J. M. Moura, "Discrete signal processing on graphs: Graph Fourier transform," in *Proc. IEEE Int. Conf. Acoust., Speech, Signal Process.*, 2013, pp. 6167–6170.
- [28] S. Furutani, T. Shibahara, M. Akiyama, K. Hato, and M. Aida, "Graph signal processing for directed graphs based on the Hermitian Laplacian," in *Proc. Mach. Learn. Knowl. Discov. Databases*. U. Brefeld, E. Fromont, A. Hotho, A. Knobbe, M. Maathuis, and C. Robardet, Eds., Cham, Switzerland: Springer-Verlag, 2020, pp. 447–463.
- [29] A. Sandryhaila and J. M. Moura, "Discrete signal processing on graphs: Frequency analysis," *IEEE Trans. Signal Process.*, vol. 62, no. 12, pp. 3042–3054, Jun. 2014.
- [30] R. Shafiqpour, A. Khodabakhsh, G. Mateos, and E. Nikolova, "A directed graph Fourier transform with spread frequency components," *IEEE Trans. Signal Process.*, vol. 67, no. 4, pp. 946–960, Feb. 2019.
- [31] S. Sardellitti, S. Barbarossa, and P. Di Lorenzo, "On the graph Fourier transform for directed graphs," *IEEE J. Sel. Topics Signal Process.*, vol. 11, no. 6, pp. 796–811, Sep. 2017.
- [32] A. Sandryhaila and J. M. Moura, "Discrete signal processing on graphs: Graph filters," in *Proc. IEEE Int. Conf. Acoust., Speech, Signal Process. (ICASSP)*. IEEE, May 2013, pp. 6163–6166.
- [33] J. Domingos and J. M. Moura, "Graph Fourier transform: A stable approximation," *IEEE Trans. Signal Process.*, vol. 68, pp. 4422–4437, 2020.
- [34] Y. Wang, B. Li, and Q. Cheng, "The fractional Fourier transform on graphs," in *Proc. Asia-Pacific Signal Inf. Process. Assoc. Annu. Summit Conf.*, Dec. 2017, pp. 105–110.
- [35] Y. Wang and B. Li, "The fractional Fourier transform on graphs: Sampling and recovery," in *Proc. 14th IEEE Int. Conf. Signal Process.*, 2018, pp. 1103–1108.
- [36] D. Wei and Z. Yan, "Generalized sampling of graph signals with prior information based on graph fractional Fourier transform," *Signal Process.*, vol. 214, p. 109263, 2024.
- [37] T. Alikashioglu, B. Kartal, and A. Koç, "Graph fractional Fourier transform: A unified theory," *IEEE Trans. Signal Process.*, vol. 72, pp. 3834–3850, 2024.
- [38] F. Yan and B. Li, "Multi-dimensional graph fractional Fourier transform and its application to data compression," *Digit. Signal Process.*, vol. 129, p. 103683, 2022.
- [39] E. Koç, T. Alikashioglu, A. C. Aras, and A. Koç, "Trainable fractional Fourier transform," *IEEE Signal Process. Lett.*, vol. 31, pp. 751–755, 2024.
- [40] F. Yan and B. Li, "Spectral graph fractional Fourier transform for directed graphs and its application," *Signal Process.*, vol. 210, p. 109099, 2023.
- [41] T. Alikashioglu, B. Kartal, E. Özgünay, and A. Koç, "Joint time-vertex fractional Fourier transform," *Signal Process.*, vol. 233, p. 109944, 2025.
- [42] F. Yan and B. Li, "Windowed fractional Fourier transform on graphs: Properties and fast algorithm," *Digit. Signal Process.*, vol. 118, p. 103210, 2021.
- [43] L. Yang, W. Meng, and X. Zhao, "Color image encryption using angular graph Fourier transform," *Int. J. Digit. Crime Forensics*, vol. 13, no. 3, pp. 59–82, 2021.
- [44] A. Gavili and X. Zhang, "On the shift operator, graph frequency, and optimal filtering in graph signal processing," *IEEE Trans. Signal Process.*, vol. 65, no. 23, pp. 6303–6318, Dec. 2017.
- [45] T. Herter and K. Lott, "Algorithms for decomposing 3-d orthogonal matrices into primitive rotations," *Comput. Graph.*, vol. 17, no. 5, pp. 517–527, 1993.
- [46] E. W. Weisstein, "Rotation matrix," *MathWorld—A Wolfram Web Resource*, 2003.
- [47] D. Gruber, "The mathematics of the 3d rotation matrix," in *Proc. Xtreme Game Developers Conf.*, 2000, pp. 1–14.
- [48] D. Q. Huynh, "Metrics for 3d rotations: Comparison and analysis," *J. Math. Imaging Vis.*, vol. 35, no. 2, pp. 155–164, 2009.
- [49] A. Kutay, H. M. Ozaktas, O. Ankan, and L. Onural, "Optimal filtering in fractional Fourier domains," *IEEE Trans. Signal Process.*, vol. 45, no. 5, pp. 1129–1143, May 1997.
- [50] C. Ozturk, H. M. Ozaktas, S. Gezici, and A. Koç, "Optimal fractional Fourier filtering for graph signals," *IEEE Trans. Signal Process.*, vol. 69, pp. 2902–2912, May 2021.
- [51] Z. Ge, H. Guo, T. Wang, and Z. Yang, "The optimal joint time-vertex graph filter design: From ordinary graph Fourier domains to fractional graph Fourier domains," *Circuits, Syst., Signal Process.*, vol. 42, no. 7, pp. 4002–4018, 2023.
- [52] USC-SIPI Image Database, <https://sipi.usc.edu/database/>.
- [53] L. Charles, Q. Cai, E. S. Orts, and A. C. Philip, "Jpeg pleno database: microsoft voxelized upper bodies—a voxelized point cloud dataset," 2021.